

PLANETARY RADAR

- I. Introduction
- II. Techniques and Instrumentation
- III. Radar Measurements and Target Properties
- IV. Prospects for Planetary Radar

Steven J. Ostro
*Jet Propulsion Laboratory,
California Institute of Technology*

GLOSSARY

- Aliasing:** Overlapping of echo at different frequencies or at different time delays.
- Antenna gain:** Ratio of an antenna’s sensitivity in the direction toward which it is pointed to its average sensitivity in all directions.
- Circular polarization ratio:** Ratio of echo power received in the same sense of circular polarization as transmitted (the SC sense) to that received in the opposite (OC) sense.
- Doppler shift:** Difference between the frequencies of the radar echo and the transmission, caused by the relative velocity of the target with respect to the radar.
- Echo bandwidth:** Dispersion in Doppler frequency of an echo, that is, the width of the echo power spectrum.
- Ephemeris:** Table of planetary positions as a function of time (plural: ephemerides).
- Klystron:** Vacuum-tube amplifier used in planetary radar transmitters.
- Radar albedo:** Ratio of a target’s radar cross section in a specified polarization to its projected area; hence, a measure of the target’s radar reflectivity.
- Radar cross section:** Most common measure of a target’s scattering efficiency, equal to the projected area of that perfect metal sphere that

- would give the same echo power as the target if observed at the target’s location.
- Scattering law:** Function giving the dependence of a surface element’s radar cross section on viewing angle.
- Synodic rotation period:** Apparent rotation period of a target that is moving relative to the observer, to be distinguished from the “sidereal” rotation period measured with respect to the fixed stars.
- Time delay:** Time between transmission of a radar signal and reception of the echo.

Planetary radar astronomy is the study of solar system entities (the Moon, asteroids, and comets, as well as the major planets and their satellites and ring systems) by transmitting a radio signal toward the target and then receiving and analyzing the echo. This field of research has primarily involved observations with Earth-based radar telescopes, but also includes certain experiments with the transmitter and/or the receiver on board a spacecraft orbiting or passing near a planetary object. However, radar studies of Earth’s surface, atmosphere, or ionosphere from spacecraft, aircraft, or the ground are not considered part of planetary radar astronomy. Radar studies of the Sun involve such distinctly individual methodologies and physical considerations that solar radar astronomy is considered a field separate from planetary radar astronomy.

I. INTRODUCTION

A. SCIENTIFIC CONTEXT

Planetary radar astronomy is a field of science at the intersection of planetology, radio astronomy, and radar engineering. A radar telescope is essentially a radio telescope equipped with a high-power radio transmitter and specialized electronic instrumentation designed to link transmitter, receiver, data-acquisition, and telescope-pointing components together in an integrated radar system. The principles underlying operation of this system are not fundamentally very different from those involved in radars used, for example, in marine and aircraft navigation, measurement of automobile speeds, and satellite surveillance. However, planetary radars must detect echoes from targets at interplanetary distances ($\sim 10^5\text{--}10^9$ km) and therefore are the largest and most powerful radar systems in existence.

The advantages of radar observations in astronomy stem from the high degree of control exercised by the observer on the transmitted signal used to illuminate the target. Whereas virtually every other astronomical technique relies on passive measurement of reflected sunlight or naturally emitted radiation, the radar astronomer controls all the properties of the illumination, including its intensity, direction, polarization, and time/frequency structure. The properties of the transmitted waveform are selected to achieve particular scientific objectives. By comparing the properties of the echo to the very well known properties of the transmission, some of the target's properties can be deduced. Hence, the observer is intimately involved in an active astronomical observation and, in a very real sense, performs a controlled laboratory experiment on the planetary target.

Radar delay-Doppler and interferometric techniques can spatially resolve a target whose angular extent is dwarfed by the antenna beamwidth, thereby bestowing a considerable advantage on radar over optical techniques in the study of asteroids, which appear like "point sources" through ground-based optical telescopes. Furthermore, by virtue of the centimeter-to-meter wavelengths employed, radar is sensitive to scales of surface structure many orders of magnitude larger than those probed in visible or infrared regions of the spectrum. Radar is also unique in its ability to "see through" the dense clouds that enshroud Venus and the glowing gaseous coma that conceals the nucleus of a comet. Because of its unique capabilities,

radar astronomy has made essential contributions to planetary exploration for a third of a century.

B. HISTORY

Radar technology was developed rapidly to meet military needs during World War II. In 1946, soon after the war's conclusion, groups in the United States and Hungary obtained echoes from the Moon, giving birth to planetary radar astronomy. These early postwar efforts were motivated primarily by interest in electromagnetic propagation through the ionosphere and the possibility for using the Moon as a "relay" for radio communication.

During the next two decades, the development of nuclear weaponry and the need for ballistic missile warning systems prompted enormous improvements in radar capabilities. This period also saw rapid growth in radio astronomy and the construction of huge radio telescopes. In 1957, the Soviet Union launched *Sputnik* and with it the space age, and in 1958, with the formation by the U.S. Congress of the National Aeronautics and Space Administration (NASA), a great deal of scientific attention turned to the Moon and to planetary exploration in general. During the ensuing years, exhaustive radar investigations of the Moon were conducted at wavelengths from 0.9 cm to 20 m, and the results generated theories of radar scattering from natural surfaces that still see wide application.

By 1963, improvements in the sensitivity of planetary radars in both the United States and the U.S.S.R. had permitted the initial detections of echoes from the terrestrial planets (Venus, Mercury, and Mars). During this period, radar investigations provided the first accurate determinations of the rotations of Venus and Mercury and the earliest indications for the extreme geologic diversity of Mars. Radar images of Venus have revealed small portions of that planet's surface at increasingly fine resolution since the late 1960s, and in 1979 the Pioneer Venus Spacecraft Radar Experiment gave us our first look at Venus's global distributions of topography, radar reflectivity, and surface slopes. During the 1980s, maps having sparse coverage but resolution down to ~ 1 km were obtained from the Soviet *Venera 15* and *16* orbiters and from ground-based observations with improved systems. Much more recently, the *Magellan* spacecraft radar revealed most of the planet's surface with unprecedented clarity, revealing a rich assortment of volcanic, tectonic, and impact features.

The first echoes from a near-Earth asteroid (1566 Icarus) were detected in 1968; it would be nearly an-

other decade before the first radar detection of a main belt asteroid (1 Ceres in 1977), to be followed in 1980 by the first detection of echoes from a comet (Encke). During 1972 and 1973, detection of 13-cm-wavelength radar echoes from Saturn's rings shattered prevailing notions that typical ring particles were 0.1 to 1.0 mm in size—the fact that decimeter-scale radio waves are backscattered efficiently requires that a large fraction of the particles be larger than a centimeter. Observations by the Voyager spacecraft confirmed this fact and further suggested that particle sizes extend to at least 10 m.

In the mid-1970s, echoes from Jupiter's Galilean satellites Europa, Ganymede, and Callisto revealed the manner in which these icy moons backscatter circularly polarized waves to be extraordinarily strange, and totally outside the realm of previous radar experience. We now understand that those echoes were due to high-order multiple scattering from within the top few decimeters of the satellites' regoliths, but there remain important questions about the geologic structures involved and the nature of electromagnetic interactions with those structures.

The late 1980s saw the initial detections of Phobos and Titan; the accurate measurement of Io's radar properties; the discovery of large-particle clouds accompanying comets; the dual-polarization mapping of Mars and the icy Galilean satellites; and radar imaging of asteroids that revealed an extraordinary assortment of radar signatures and several highly irregular shapes, including a "contact-binary" near-Earth asteroid.

During the 1990s, the novel use of instrumentation and waveforms has yielded the first full-disk radar images of the terrestrial planets, revealing the global diversity of small-scale morphology on these objects and the surprising presence of radar-bright polar anomalies on Mercury as well as Mars. Similarities between the polarization and albedo signatures of these features and those of the icy Galilean satellites argue persuasively that Mercury's polar anomalies are deposits of water ice in the floors of craters that are perpetually shaded from sunlight by Mercury's low obliquity. The first time-delay-resolved ("ranging") measurements to Ganymede and Callisto were carried out in 1992. That same year, delay-Doppler images of the closely approaching asteroid 4179 Toutatis revealed this strange object to be in a very slow, non-principal-axis spin state and provided the first geologically detailed pictures of an Earth-orbit-crossing asteroid. This decade also saw the first intercontinental radar observations and the beginning of planetary radar in Germany and Japan. By 1997, the list of small planetary objects detected by radar included 6 comets, 37 main belt asteroids, and 47 near-Earth asteroids (Table I).

Perhaps the most far-reaching recent development is the upgrading of the Arecibo telescope's sensitivity by over an order of magnitude. At this writing, Arecibo is about to return to operation, and radar astronomy is poised to begin a new era of major contributions to planetary science.

II. TECHNIQUES AND INSTRUMENTATION

A. ECHO DETECTABILITY

How close must a planetary target be for its radar echo to be detectable? For a given transmitted power P_T and antenna gain G , the power flux a distance R from the radar will be $P_T G / 4\pi R^2$. We define the target's radar cross section, σ , as 4π times the backscattered power per unit of solid angle per unit of flux incident at the target. Then, letting λ be the radar wavelength and defining the antenna's effective aperture as $A = G\lambda^2/4\pi$, we have the received power

$$P_R = P_T G A \sigma / (4\pi)^2 R^4 \quad (1)$$

This power might be much less than the receiver noise power, $P_N = k T_S \Delta f$, where k is Boltzmann's constant, T_S is the receiver system temperature, and Δf is the frequency resolution of the data. However, the mean level of P_N constitutes a background that can be determined and removed, so P_R will be detectable as long as it is at least several times larger than the standard deviation of the random fluctuations in P_N . These fluctuations can be shown to have a distribution that, for usual values of Δf and the integration time Δt , is nearly Gaussian with standard deviation $\Delta P_N = P_N / (\Delta f \Delta t)^{1/2}$. The highest signal-to-noise ratio, or $\text{SNR} = P_R / \Delta P_N$, will be achieved for a frequency resolution equal to the effective bandwidth of the echo. As discussed in the following, that bandwidth is proportional to $D/\lambda P$, where D is the target's diameter and P is the target's rotation period, so let us assume that $\Delta f \sim D/\lambda P$. By writing $\sigma = \hat{\sigma} \pi D^2/4$, where the radar albedo $\hat{\sigma}$ is a measure of the target's radar reflectivity, we arrive at the following expression for the echo's signal-to-noise ratio:

$$\text{SNR} \sim (\text{system factor})(\text{target factor}(\Delta t)^{1/2}) \quad (2)$$

TABLE I
Radar-Detected Planetary Targets

Year of first detection	Planets, satellites, rings	Main belt asteroids	Near-Earth asteroids	Comets
1946	Moon			
1961	Venus			
1962	Mercury			
1963	Mars			
1968			1566 Icarus	
1972			1685 Toro	
1973	Saturn's rings			
1974	Ganymede			
1975	Callisto Europa		433 Eros	
1976	Io		1580 Betulia	
1977		1 Ceres		
1979		4 Vesta		
1980		7 Iris 16 Psyche	1862 Apollo	Encke
1981		97 Klotho 8 Flora	1915 Quetzalcoatl 2100 Ra-Shalom	
1982		2 Pallas 12 Victoria 19 Fortuna 46 Hestia		Grigg-Skjellerup
1983		5 Astraea 139 Juewa 356 Liguria 80 Sappho 694 Ekard	1620 Geographos 2201 Oljato	IRAS-Araki-Alcock Sugano-Saigusa-Fujikawa
1984		9 Metis 554 Peraga 144 Vibia	2101 Adonis	
1985		6 Hebe 41 Daphne 21 Lutetia 33 Polyhymnia 84 Klio 192 Nausikaa 230 Athamantis 216 Kleopatra 18 Melpomene	1627 Ivar 1036 Ganymed 1866 Sisypheus	Halley
1986		393 Lampetia 27 Euterpe	6178 1986DA 1986JK 3103 Eger (1982BB) 3199 Nefertiti	
1987		532 Herculina 20 Massalia	1981 Midas 3757 1982XB	
1988	Phobos	654 Zelinda 105 Artemis	3908 1980PA	
1989	Titan		4034 1986PA 1989JA 4769 Castalia (1989PB) 1917 Cuyo	

continues

continued

Year of first detection	Planets, satel- lites, rings	Main belt asteroids	Near-Earth asteroids	Comets
1990		78 Diana 194 Prokne	1990MF 1990OS 4544 Xanthus (1989FB)	
1991		324 Bamberga 796 Sarita	1991AQ 6489 Golevka (1991JX) 1991EE	
1992			5189 1990UQ 4179 Toutatis	
1994			4953 1990MU	
1995			2062 Aten (1976AA)	
1996			1992QN 1993QA 2063 Bacchus 1996JG 1991CS 4197 1982TA	Hyakutake (C/1996 B2)
1997			7341 1991VK 7482 1994PC1 1997BR 1998BY7	
1998			6037 1988EG 4183 Cuno 1998KY26	

where

$$\begin{aligned} \text{system factor} &\sim P_{\text{T}}A^2/\lambda^{3/2}T_{\text{s}} \\ &\sim P_{\text{T}}G^2\lambda^{5/2}/T_{\text{s}} \end{aligned}$$

(3)

and

$$\text{target factor} \sim \hat{\sigma}D^{3/2}P^{1/2}/R^4$$

(4)

The inverse-fourth-power dependence of SNR on target distance is a severe limitation in ground-based observations, but it can be overcome by constructing very powerful radar systems.

B. RADAR SYSTEMS

The world has two active planetary radar facilities: the Arecibo Observatory (part of the National Astronomy and Ionosphere Center) in Puerto Rico and the Goldstone Solar System Radar in California. Radar wavelengths are 13 cm and 70 cm for Arecibo and 3.5 cm and 13 cm for Goldstone; with each instrument, enormously more sensitivity is achievable with the shorter wavelength. The upgraded Arecibo telescope has twice the range and will see three times the volume of Goldstone, whereas Goldstone sees twice as much sky as Arecibo and can track targets at least three times

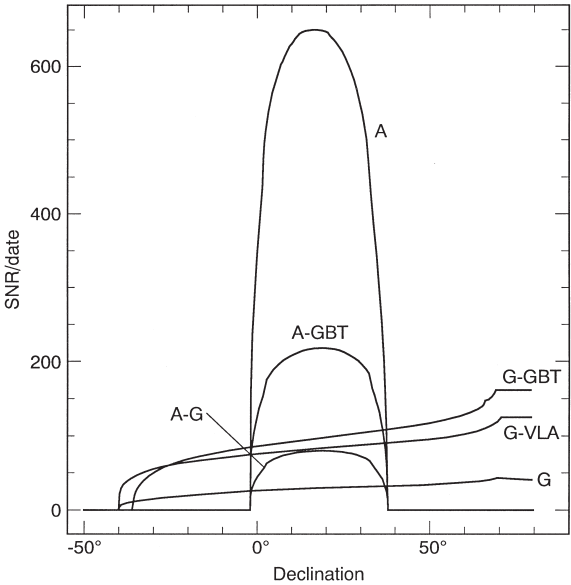


FIGURE 1 Sensitivities of planetary radar systems. Curves plot the single-date, signal-to-noise ratio of echoes from a typical 1-km asteroid ($\hat{\sigma} = 0.1$, $P = 5$ hr) at a distance of 0.1 AU for the upgraded Arecibo telescope (A), Goldstone (G), and bistatic configurations using those instruments and the Very Large Array (VLA) or the Greenbank Telescope (GBT).



FIGURE 2 The Arecibo Observatory in Puerto Rico. (a) Aerial view prior to the recent upgrade. The diameter of the spherical reflector is 305 m. (b) A close-up view of the structure suspended above the reflector, showing the old 430-MHz line feed and the radome that encloses the new Gregorian secondary and tertiary subreflectors.

longer. Figure 1 shows the relative sensitivities of planetary radar systems as a function of target declination.

The Arecibo telescope (Fig. 2) consists of a 305-m-diameter, fixed reflector whose surface is a 51-m-deep section of a 265-m-radius sphere. Moveable feeds designed to correct for spherical aberration are suspended from a triangular platform 137 m above the reflector and can be aimed toward various positions on the reflector, enabling the telescope to point within about 20 degrees of the overhead direction (declination 18.3°N). Components of the recent upgrade have included a megawatt transmitter, a ground screen to reduce noise generated by radiation from the ground, and replacement of most of the old single-frequency line feeds with a Gregorian reflector system (named after the seventeenth-century mathematician James Gregory) that employs 22-m secondary and 8-m tertiary subreflectors enclosed inside a 26-m dome.

The Goldstone main antenna, DSS-14 (DSS stands for Deep Space Station), is part of the NASA Deep Space Network, which is run by the Jet Propulsion Laboratory (JPL). It is a fully steerable, 70-m, parabolic reflector (Fig. 3). Bistatic (two-station) experiments employing transmission from DSS-14 and re-

ception of echoes at the 27-antenna Very Large Array (VLA) in New Mexico have synthesized a beamwidth as small as 0.24 seconds of arc, versus 2 minutes of arc for single-dish observations with Arecibo or Goldstone. Bistatic experiments using DSS-14 transmissions and reception of echoes at DSS-13, a 34-m antenna 22 km away, have been conducted on several very close targets. In coming years, bistatic observations between Arecibo and Goldstone, or using transmission from Arecibo or Goldstone and reception at the 100-m Greenbank Telescope, now under construction in West Virginia, should prove advantageous for outer planet satellites and nearby asteroids and comets.

Figure 4 is a simplified block diagram of a planetary radar system. A waveguide switch, a moveable subreflector, or a moveable mirror system is used to place the antenna in a transmitting or receiving configuration. The heart of the transmitter is one or two klystron vacuum-tube amplifiers. In these tubes, electrons accelerated by a potential drop of some 60 kV are magnetically focused as they enter the first of five or six cavities. In this first cavity, an oscillating electric field at a certain radio frequency (RF, e.g., 2380 MHz for Arecibo) modulates the electrons' velocities and hence

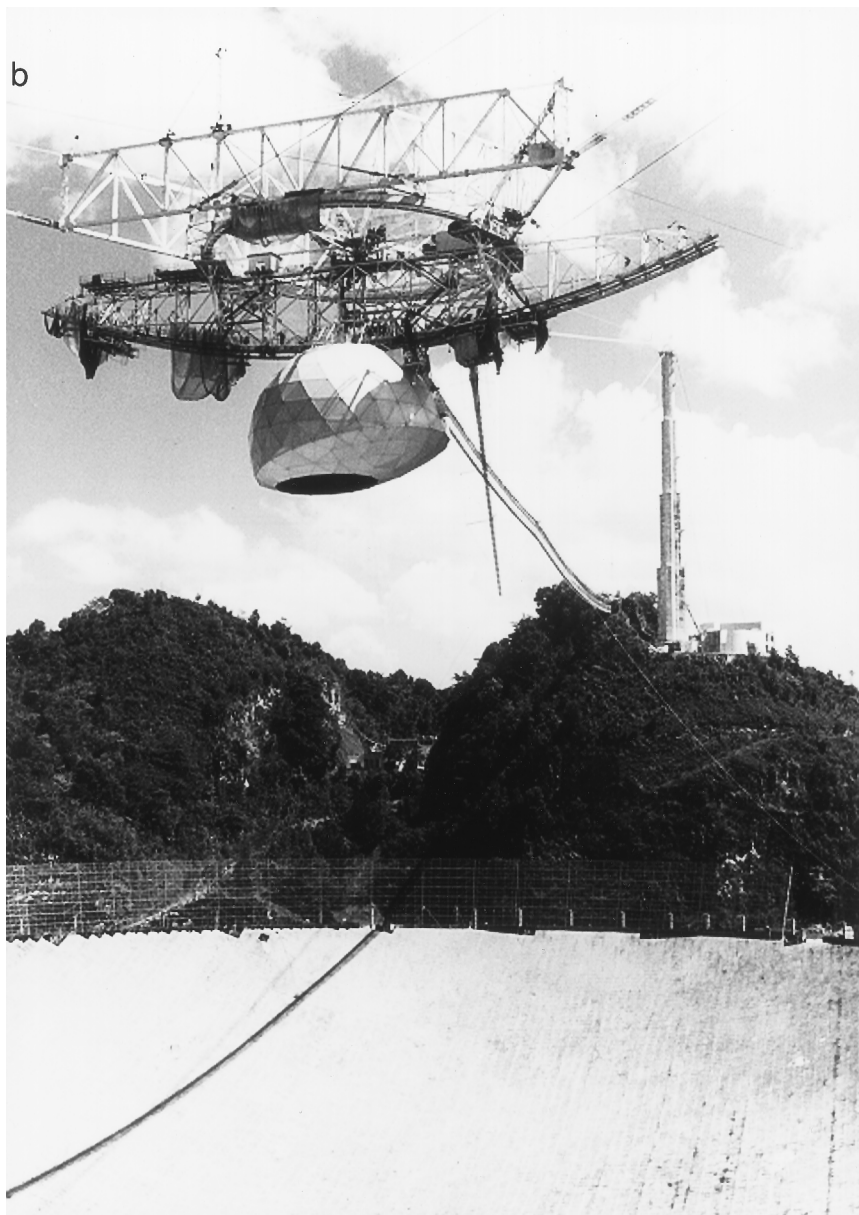


FIGURE 2 (continued)

their density and energy flux. Subsequent resonant cavities enhance this velocity bunching (they constitute what is called a “cascade amplifier”) and about half of the input DC power is converted to RF power and sent out through a waveguide to the antenna feed system and radiated toward the target. The other half of the input power is waste heat and must be transported away from the klystron by cooling water. The impact of the electrons on the collector anode generates dangerous X rays that must be contained by heavy metal shielding surrounding the tube, a requirement that

further boosts the weight, complexity, and hence cost of a high-power transmitter.

In most single-antenna observations, one transmits for a duration near the roundtrip propagation time to the target (i.e., until the echo from the beginning of the transmission is about to arrive), and then receives for a similar duration. In the “front end” of the receiving system, the echo signal is amplified by a maser and converted from RF frequencies (e.g., 2380 MHz for Arecibo at 13 cm) down to intermediate frequencies (IF, e.g., 30 MHz), for which transmission line losses

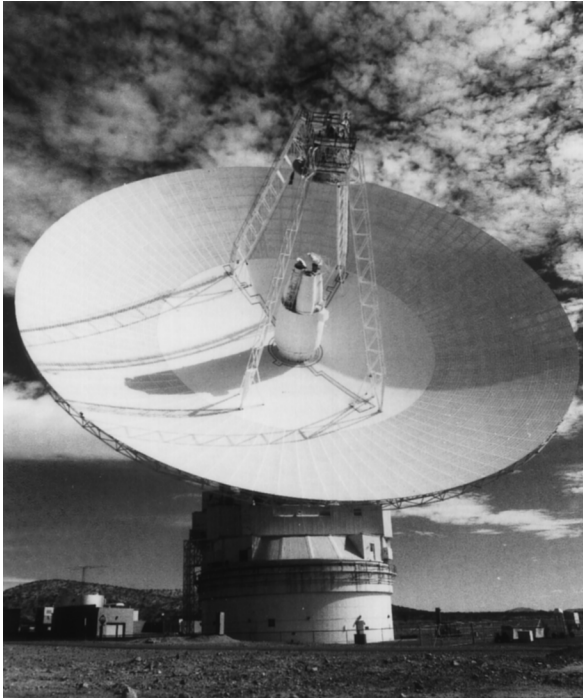


FIGURE 3 The 70-m Goldstone Solar System Radar antenna, DSS-14, in California.

are small, and passed from the proximity of the antenna feed to a remote control room containing additional stages of signal-processing equipment, computers, and digital tape recorders. The signal is filtered, amplified, and converted to frequencies low enough for analog voltage samples to be digitized and recorded. The frequency down-conversion can be done in several stages using analog devices called superheterodyne mixers, but in recent years it has become possible to do this digitally, at increasingly higher frequencies. The nature of the final processing prior to recording of data on a hard disk or magnetic tape depends on the nature of the radar experiment and particularly on the time/frequency structure of the transmitted waveform. Each year, systems for reducing and displaying echoes in “real time” and techniques for processing recorded data are becoming more ambitious as computers get faster.

C. ECHO TIME DELAY AND DOPPLER FREQUENCY

The time between transmission of a radar signal and reception of the echo is called the echo’s roundtrip time delay, τ , and is of order $2R/c$, where c is the speed

of light, $299,792,458 \text{ m sec}^{-1}$. Since planetary targets are not points, even an infinitesimally short transmitted pulse would be dispersed in time delay, and the total extent $\Delta\tau_{\text{TARGET}}$ of the distribution $\sigma(\tau)$ of echo power (in units of radar cross section) would be D/c for a sphere of diameter D and in general depends on the target’s size and shape.

The translational motion of the target with respect to the radar introduces a Doppler shift, ν , in the frequency of the transmission. Both the time delay and the Doppler shift of the echo can be predicted in advance from the target’s ephemeris, which is calculated using the geodetic position of the radar and the orbital elements of Earth and the target. The predicted Doppler shift can be removed electronically by continuously tuning the local oscillator used for RF-to-IF frequency conversion (see Fig. 4). The predicted Doppler must be accurate enough to avoid smearing out the echo in delay, and this requirement places stringent demands on the quality of the observing ephemeris. Time and frequency measurements are critical, because the delay/Doppler distribution of echo power is the source of the finest spatial resolution, and also because delay and Doppler are fundamental dynamical observables. Reliable, precise time/frequency measurements are made possible by high-speed data acquisition systems and stable, accurate clocks and frequency standards.

Because different parts of the rotating target will have different velocities relative to the radar, the echo will be dispersed in Doppler frequency as well as in time delay. The basic strategy of any radar experiment always involves measurement of some characteristic(s) of the function $\sigma(\tau, \nu)$, perhaps as a function of time and perhaps using more than one combination of transmitted and received polarizations. Ideally, one would like to obtain $\sigma(\tau, \nu)$ with very fine resolution, sampling that function within intervals whose dimensions, $\Delta\tau \times \Delta\nu$, are minute compared to the echo dispersions $\Delta\tau_{\text{TARGET}}$ and $\Delta\nu_{\text{TARGET}}$. However, one’s ability to resolve $\sigma(\tau, \nu)$ is necessarily limited by the available echo strength. Furthermore, as described in the next section, an intrinsic upper bound on the product $\Delta\tau \Delta\nu$ forces a trade-off between delay resolution and Doppler resolution for the most efficient waveforms used. Under these constraints, many planetary radar experiments employ waveforms aimed at providing estimates of one of the marginal distributions, $\sigma(\tau)$ or $\sigma(\nu)$. Figure 5 shows the geometry of delay-resolution cells and Doppler-resolution cells for a spherical target and sketches the relation between these cells and $\sigma(\tau)$ and $\sigma(\nu)$. Delay-Doppler measurements are explored further in the following.

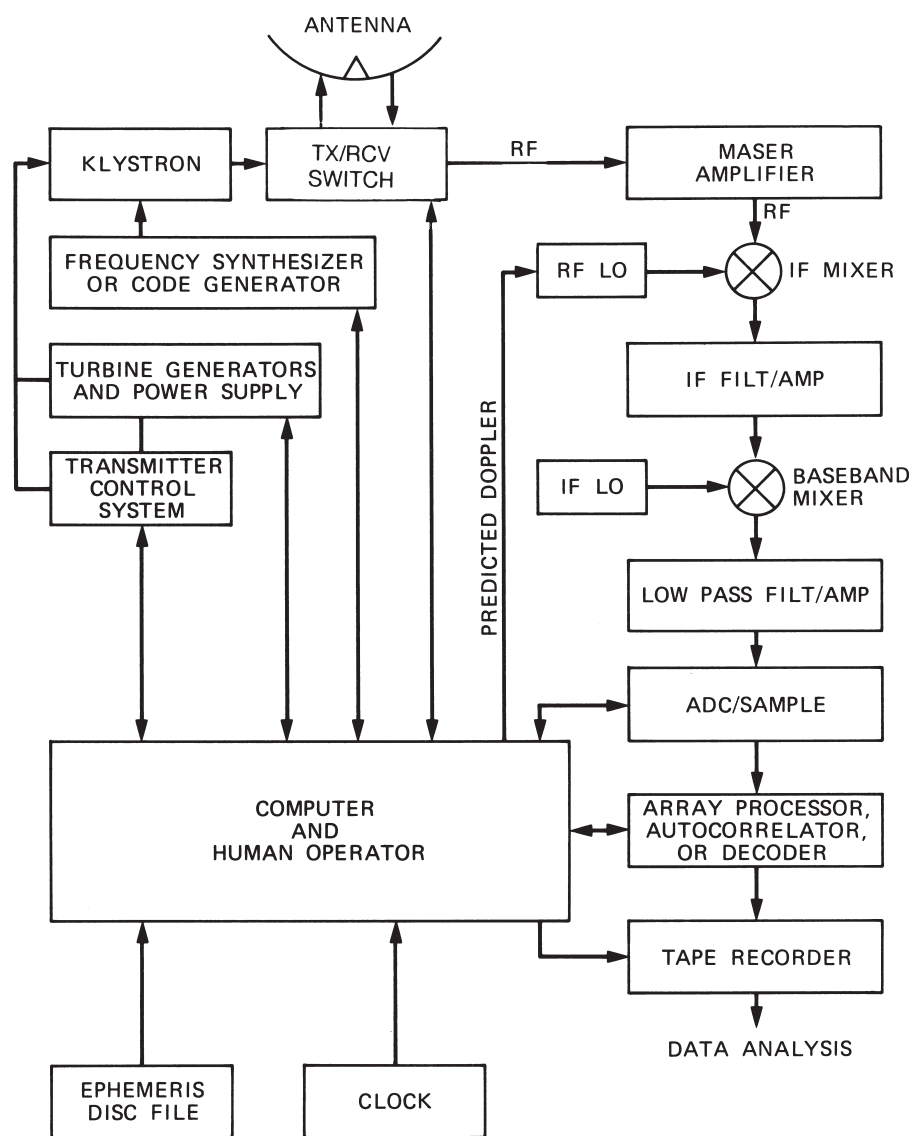


FIGURE 4 Block diagram of a planetary radar system. RF LO and IF LO denote radio frequency and intermediate frequency local oscillators, and ADC denotes analog-to-digital converter.

D. RADAR WAVEFORMS

In the simplest radar experiment, the transmitted signal is a highly monochromatic, unmodulated continuous-wave (cw) signal. Analysis of the received signal comprises Fourier transformation of a series of time samples and yields an estimate of the echo power spectrum $\sigma(\nu)$, but contains no information about the distance to the target or $\sigma(\tau)$. To avoid aliasing, the sampling rate must be at least as large as the bandwidth of the low-pass filter (see Fig. 4) and usually is comparable to or larger than the echo's intrinsic dispersion

$\Delta\nu_{\text{TARGET}}$ from Doppler broadening. Fast-Fourier transform (FFT) algorithms, implemented via software or hard-wired (e.g., in an array processor), greatly speed the calculation of discrete spectra from time series, and are ubiquitous in radar astronomy. In a single FFT operation, a string of N time samples taken at intervals of Δt seconds is transformed into a string of N spectral elements with frequency resolution $\Delta\nu = 1/N \Delta t$. Most planetary radar targets are sufficiently narrowband for power spectra to be computed, accumulated, and recorded directly on magnetic tape at convenient intervals. In some situations, it is desirable

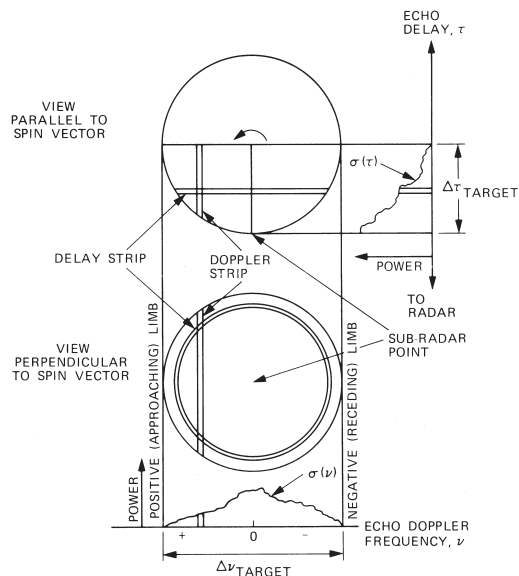


FIGURE 5 Time-delay and Doppler-frequency resolution of the radar echo from a rotating spherical target.

to record time samples on tape and Fourier-analyze the data later, perhaps using FFTs of different lengths to obtain spectra at a variety of frequency resolutions. In others, it is convenient to pass the signal through an autocorrelator to record autocorrelation functions, and then apply FFTs to extract spectra.

To obtain delay resolution, one must apply some sort of time modulation to the transmitted waveform. For example, a short-duration pulse of cw signal lasting 1 μ sec would provide delay resolution of 150 m. However, the echo would have to compete with the noise power in a bandwidth of order 1 MHz so the echo power from many consecutive pulses would probably have to be summed to yield a detection. One would not want these pulses to be too close together, however, or there would be more than one pulse incident on the target at once and interpretation of echoes would be insufferably ambiguous. Thus, one arranges the pulse repetition period t_{PRP} to exceed the target's intrinsic delay dispersion $\Delta\tau_{\text{TARGET}}$, ensuring that the echo will consist of successive, nonoverlapping "replicas" of $\sigma(\tau)$ separated from each other by t_{PRP} . To generate this "pulsed cw" waveform, the transmitter is switched on and off while the frequency synthesizer (see Fig. 4) maintains phase coherence from pulse to pulse. Then Fourier transformation of time samples taken at the same position within each of N successive replicas of $\sigma(\tau)$ yields the power spectrum of echo from a certain delay resolution cell on the target. This spectrum has an unaliased bandwidth of $1/t_{\text{PRP}}$ and a frequency resolution of $1/Nt_{\text{PRP}}$. Repeating this process for a different position within each replica of $\sigma(\tau)$ yields the power spectrum for echo from a different delay resolution

cell, and in this manner one obtains the delay-Doppler image $\sigma(\tau, \nu)$.

In practice, instead of pulsing the transmitter, one usually codes a cw signal with a sequence of 180° phase reversals and cross-correlates the echo with a representation of the code (e.g., using the decoder in Fig. 4), thereby synthesizing a pulse train with the desired values of Δt and t_{PRP} . With this approach, one optimizes SNR, because it is much cheaper to transmit the same average power continuously than by pulsing the transmitter. Most modern ground-based radar astronomy observations employ cw or repetitive, phase-coded cw waveforms.

A limitation of coherent-pulsed or repetitive, binary-phase-coded cw waveforms follows from combining the requirement that there never be more than one echo received from the target at any instant (i.e., that $t_{\text{PRP}} > \Delta\tau_{\text{TARGET}}$) with the antialiasing frequency requirement that the rate ($1/t_{\text{PRP}}$) at which echo from a given delay resolution cell is sampled be no less than the target bandwidth $\Delta\nu_{\text{TARGET}}$. Therefore, a target must satisfy $\Delta\tau_{\text{TARGET}} \Delta\nu_{\text{TARGET}} \leq 1$ or it is "overspread" (Table II) and cannot be investigated completely and simultaneously in delay and Doppler without aliasing, at least with the waveforms discussed so far. Various degrees of aliasing may be "acceptable" for overspread factors less than about 10, depending on the precise experimental objectives and the exact properties of the echo.

How can the full delay-Doppler distribution be obtained for overspread targets? Frequency-swept and frequency-stepped waveforms have seen limited use in planetary radar; the latter approach was applied to Saturn's rings. A new technique uses a nonrepeating, binary-phase-coded cw waveform. The received signal for any given delay cell is decoded by multiplying it by a suitably lagged replica of the code. Developed for observations of the highly overspread ionosphere, this "coded-long-pulse" or "random-code" waveform redistributes delay-aliased echo power into an additive white-noise background. The SNR is reduced accordingly, but this penalty is acceptable for strong targets.

III. RADAR MEASUREMENTS AND TARGET PROPERTIES

A. ALBEDO AND POLARIZATION RATIO

A primary goal of the initial radar investigation of any planetary target is estimation of the target's radar cross

TABLE II
Characteristics of Selected Planetary Radar Targets^a

Target	Minimum echo delay ^b (min)	Radar cross section (km ²)	Radar albedo $\hat{\sigma}_o$	Circular polarization ratio, μ_c	Maximum dispersions ^c		
					Delay (msec)	Doppler (Hz)	Product
Moon	0.04	6.6×10^5	0.07	0.1	12	60	0.7
Mercury	9.1	1.1×10^6	0.06	0.1	16	110	2
Venus	4.5	1.3×10^7	0.11	0.1	40	110	4
Mars	6.2	2.9×10^6	0.08	0.3	23	7600	170
Phobos	6.2	22	0.06	0.1	0.1	100	10^{-2}
1 Ceres	26	2.7×10^4	0.05	0.0	3	3100	9
2 Pallas	25	1.7×10^4	0.08	0.0	2	2000	4
12 Victoria	15	2.3×10^3	0.22	0.1	0.5	590	3
16 Psyche	28	1.4×10^4	0.31	0.1	0.8	2200	2
216 Kleopatra	20	7.1×10^3	0.44	0.0	?	750	?
324 Bamberga	13	2.9×10^3	0.06	0.1	0.8	230	0.2
1685 Toro	2.3	1.7	0.1	0.2	0.02	14	10^{-4}
1862 Apollo	0.9	0.2	0.1	0.4	0.01	16	10^{-4}
2100 Ra-Shalom	3.0	1.0	0.1	0.2	0.01	5	10^{-4}
2101 Adonis	1.5	0.02	<0.3	1.0	?	2	?
4179 Toutatis	0.4	1.3	0.24	0.3	0.01	1	10^{-5}
4769 Castalia	0.6	0.2	0.15	0.3	0.01	10	10^{-4}
6178 1986DA	3.4	2.4	0.6	0.1	12	15	0.2
IAA ^d nucleus	0.5	2.4	0.04?	0.1	?	4	?
IAA coma	0.5	0.8	?	0.01	?	600	?
HYA ^e nucleus	1.7	0.11	?	0.5	?	12	?
HYA coma	1.7	1.3	?	<1	?	3000	?
Io	66	2×10^6	0.2	0.5	12	2400	29
Europa	66	8×10^6	1.0	1.5	10	1000	11
Ganymede	66	1×10^7	0.6	1.4	18	850	15
Callisto	66	5×10^6	0.3	1.2	16	330	5
Saturn's rings	134	10^8 – 10^9	0.7	0.5	1600	6×10^5	10^6

^a Typical 3.5- to 13-cm values. Question marks denote absence of radar data or of prior information about target dimensions.
^b For asteroids and comets, this is the minimum echo time delay for radar observations to date.
^c Doppler dispersion for transmitter frequency of 2380 MHz (λ 13 cm). The product of the dispersions in delay and Doppler is the overspread factor at 2380 MHz.
^d IAA denotes comet IRAS-Araki-Alcock.
^e HYA denotes comet Hyakutake (C/1996 B2).

section, σ , and its normalized radar cross section or “radar albedo,” $\hat{\sigma} = \sigma/A_p$, where A_p is the target’s geometric projected area. Since the radar astronomer selects the transmitted and received polarizations, any estimate of σ or $\hat{\sigma}$ must be identified accordingly. The most common approach is to transmit a circularly polarized wave and to use separate receiving systems for simultaneous reception of the same sense of circular polarization as transmitted (i.e., the SC sense) and the opposite (OC) sense. The handedness of a circularly polarized wave is reversed on normal reflection from a smooth dielectric interface, so the OC sense dominates echoes from targets that look smooth at the radar wavelength. In this context, a surface with minimum radius

of curvature very much larger than λ would “look smooth.” SC echo power can arise from single scattering from rough surfaces, multiple scattering from smooth surfaces or subsurface heterogeneities (e.g., particles or voids), or certain subsurface refraction effects. The circular polarization ratio, $\mu_C = \sigma_{SC}/\sigma_{OC}$, is thus a useful measure of near-surface structural complexity or “roughness.” When linear polarizations are used, it is convenient to define the ratio $\mu_L = \sigma_{OL}/\sigma_{SL}$, which would be close to zero for normal reflection from a smooth dielectric interface. For all radar-detected planetary targets, $\mu_L < 1$ and $\mu_L < \mu_C$. Although the OC radar albedo, $\hat{\sigma}_{OC}$, is the most widely used gauge of radar reflectivity, some radar measurements are reported in terms of the total power (OC + SC = OL + SL) radar albedo $\hat{\sigma}_T$, which is four times the geometric albedo used in optical planetary astronomy. A smooth metallic sphere would have $\hat{\sigma}_{OC} = \hat{\sigma}_{SL} = 1$, a geometric albedo of 0.25, and $\mu_C = \mu_L = 0$.

If μ_C is close to zero (see Table II), its physical interpretation is unique, as the surface must be smooth at all scales within about an order of magnitude of λ and there can be no subsurface structure at those scales within several $1/e$ power absorption lengths, L , of the surface proper. In this special situation, we may interpret the radar albedo as the product $g\rho$, where ρ is the Fresnel power-reflection coefficient at normal incidence and the backscatter gain g depends on target shape, the distribution of surface slopes with respect to that shape, and target orientation. For most applications to date, g is $<10\%$ larger than unity, so the radar albedo provides a reasonable first approximation to ρ . Both ρ and L depend on very interesting characteristics of the surface material, including bulk density, porosity, particle size distribution, and metal abundance.

If μ_C is ~ 0.3 (e.g., Mars and some near-Earth asteroids), then much of the echo arises from some backscattering mechanism other than single, coherent reflections from large, smooth surface elements. Possibilities include multiple scattering from buried rocks or from the interiors of concave surface features such as craters, or reflections from very jagged surfaces with radii of curvature much less than a wavelength. Most planetary targets have values of $\mu_C < 0.3$ at decimeter wavelengths, so their surfaces are dominated by a component that is smooth at centimeter to meter scales.

The observables $\hat{\sigma}_{OC}$ and μ_C are disk-integrated quantities, derived from integrals of $\sigma(\nu)$ or $\sigma(\tau)$ in specific polarizations. Later, we will see how their physical interpretation profits from knowledge of the functional forms of $\sigma(\nu)$ and $\sigma(\tau)$.

B. DYNAMICAL PROPERTIES FROM DELAY/DOPPLER MEASUREMENTS

Consider radar observation of a point target a distance R from the radar. As noted earlier, the “roundtrip time delay” between transmission of a pulse toward the target and reception of the echo would be $\tau = 2R/c$. It is possible to measure time delays to within 10^{-7} sec. Actual delays encountered range from $2\frac{1}{2}$ s for the Moon to $2\frac{1}{2}$ hr for Saturn’s rings. For a typical target distance ~ 1 astronomical unit (AU), the time delay is ~ 1000 sec and can be measured with a fractional timing uncertainty of 10^{-9} , that is, with the same fractional precision as the definition of the speed of light.

If the target is in motion and has a line-of-sight component of velocity toward the radar of v_{LOS} , the target will “see” a frequency that, to first order in v_{LOS}/c , equals $f_{TX} + (v_{LOS}/c)f_{TX}$, where f_{TX} is the transmitter frequency. The target reradiates the Doppler-shifted signal, and the radar receives echo whose frequency is, again to first order, given by

$$f_{TX} + 2(v_{LOS}/c)f_{TX}$$

That is, the total Doppler shift in the received echo is

$$2v_{LOS}f_{TX}/c = v_{LOS}/(\lambda/2)$$

so a 1-Hz Doppler shift corresponds to a velocity of half a wavelength per second (e.g., 6.3 cm sec^{-1} for $\lambda 12.6 \text{ cm}$). It is not difficult to measure echo frequencies to within 0.01 Hz, so v_{LOS} can be estimated with a precision finer than 1 mm sec^{-1} . Actual values of v_{LOS} for planetary radar targets can be as large as several tens of kilometers per second, so radar velocity measurements have fractional errors as low as 10^{-8} . At this level, the second-order (special relativistic) contribution to the Doppler shift becomes measurable; in fact, planetary radar observations have provided the initial experimental verification of the second-order term.

By virtue of their high precision, radar measurements of time delay and Doppler frequency are very useful in refining our knowledge of various dynamical quantities. The first delay-resolved radar observations of Venus, during 1961–1962, yielded an estimate of the light-second equivalent of the astronomical unit that was accurate to one part in 10^6 , constituting a thousandfold improvement in the best results achieved with optical observations alone. Subsequent radar observations provided additional refinements of nearly two more orders of magnitude. In addition to determining the scale of the solar system precisely, these observations greatly improved our knowledge of the

orbits of Earth, Venus, Mercury, and Mars, and were essential for the success of the first interplanetary missions. Radar observations still contribute to maintaining the accuracy of planetary ephemerides for objects in the inner solar system, and have played an important role in dynamical studies of Jupiter's Galilean satellites. For newly discovered near-Earth asteroids, whose orbits must be estimated from optical astrometry that spans short arcs, a few radar observations can mean the difference between successfully recovering the object during its next close approach and losing it entirely. Even for near-Earth asteroids with secure orbits, delay-Doppler measurements can shrink the positional error ellipsoid significantly for decades or even centuries.

Precise interplanetary time-delay measurements have allowed increasingly decisive tests of physical theories for light, gravitational fields, and their interactions with matter and each other. For example, radar observations verify general relativity theory's prediction that for radar waves passing nearby the Sun, echo time delays are increased because of the distortion of space by the Sun's gravity. The extra delay would be $\sim 100 \mu\text{sec}$ if the angular separation of the target from the Sun were several degrees. (The Sun's angular diameter is about half a degree.) Since planets are not point targets, their echoes are dispersed in delay and Doppler, and the refinement of dynamical quantities and the testing of physical theories are tightly coupled to estimation of the mean radii, the topographic relief, and the radar scattering behavior of the targets. The key to this entire process is resolution of the distributions of echo power in delay and Doppler. In the next section, we will consider inferences about a target's dimensions and spin vector from measurements of the dispersions ($\Delta\tau_{\text{TARGET}}$, $\Delta\nu_{\text{TARGET}}$) of the echo in delay and Doppler. Then we will examine the physical information contained in the functional forms of the distributions $\sigma(\tau)$, $\sigma(\nu)$, and $\sigma(\tau, \nu)$.

C. DISPERSION OF ECHO POWER IN DELAY AND DOPPLER

Each backscattering element on a target's surface returns echo with a certain time delay and Doppler frequency (see Fig. 5). Since parallax effects and the curvature of the incident wave front are negligible for most ground-based observations (but not necessarily for observations with spacecraft), contours of constant delay are intersections of the surface with planes perpendicular to the line of sight. The point on the surface with the shortest echo time delay is called the subradar

point; the longest delays generally correspond to echoes from the planetary limbs. As noted already, the difference between these extreme delays is called the dispersion, $\Delta\tau_{\text{TARGET}}$, in $\sigma(\tau)$ or simply the "delay depth" of the target.

If the target appears to be rotating, the echo will be dispersed in Doppler frequency. For example, if the radar has an equatorial view of a spherical target with diameter D and rotation period P , then the difference between the line-of-sight velocities of points on the equator at the approaching and receding limbs would be $2\pi D/P$. Thus the dispersion of $\sigma(\nu)$ would be $\Delta\nu_{\text{TARGET}} = 4\pi D/\lambda P$. This quantity is called the bandwidth, B , of the echo power spectrum. If the view is not equatorial, the bandwidth is simply $(4\pi D \sin \alpha)/\lambda P$, where the "aspect angle" α is the acute angle between the instantaneous spin vector and the line of sight. Thus, a radar bandwidth measurement furnishes a joint constraint on the target's size, rotation period, and pole direction.

In principle, echo bandwidth measurements obtained for a sufficiently wide variety of directions can yield all three scalar coordinates of the target's intrinsic (i.e., sidereal) spin vector \mathbf{W} . This capability follows from the fact that the apparent spin vector \mathbf{W}_{app} is the vector sum of \mathbf{W} and the contribution ($\mathbf{W}_{\text{sky}} = \dot{\mathbf{e}} \times \mathbf{e}$, where the unit vector \mathbf{e} points from the target to the radar) from the target's plane-of-sky motion. Variations in \mathbf{e} , $\dot{\mathbf{e}}$, and hence \mathbf{W}_{sky} , all of which are known, lead to measurement of different values of $\mathbf{W}_{\text{app}} = \mathbf{W} + \mathbf{W}_{\text{sky}}$, permitting unique determination of all three scalar components of \mathbf{W} .

These principles were applied in the early 1960s to yield the first accurate determination of the rotations of Venus and Mercury (Fig. 6). Venus's rotation is retrograde with a 243-day sidereal period that is close to the value (243.16 days) characterizing a resonance with the relative orbits of Earth and Venus, wherein Venus would appear from Earth to rotate exactly four times between successive inferior conjunctions with the Sun. However, two decades of ground-based observations and ultimately images obtained by the *Magellan* spacecraft while in orbit around Venus have conclusively demonstrated nonresonance rotation: the period is 243.0185 ± 0.0001 days. To date, a satisfactory explanation for Venus's curious spin state is lacking.

For Mercury, long imagined on the basis of optical observations to rotate once per 88-day revolution around the Sun, radar bandwidth measurements (see Fig. 6) demonstrated direct rotation with a period (59 days) equal to two-thirds of the orbital period. This spin-orbit coupling is such that during two Mercury years, the planet rotates three times with respect to

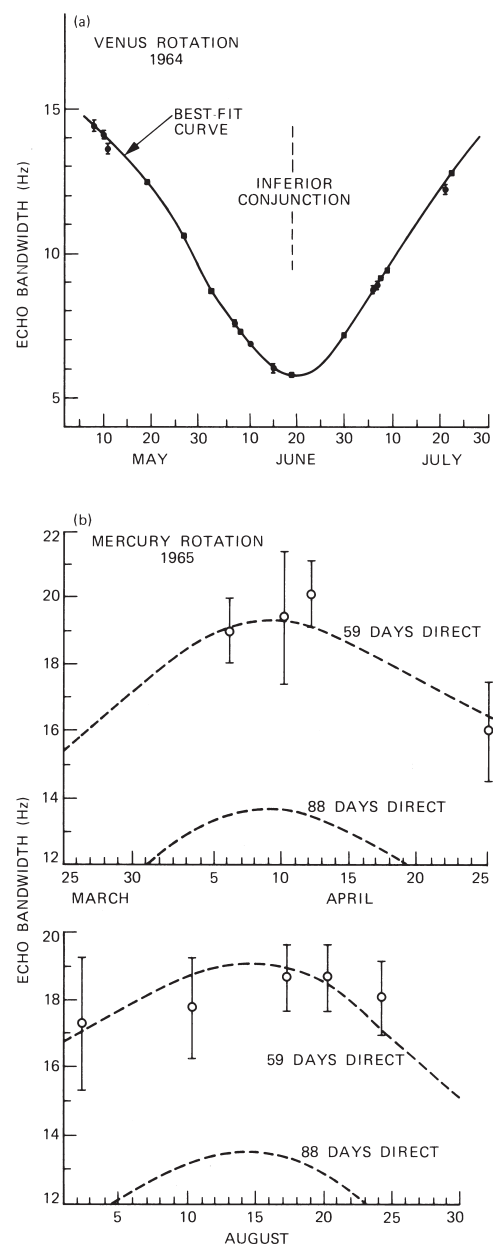


FIGURE 6 Measurements of echo bandwidth (i.e., the dispersion of echo power in Doppler frequency) used to determine the rotations of (a) Venus and (b) Mercury. [From R. B. Dyce, G. H. Pettengill, and I. I. Shapiro (1967). *Astron. J.* 72, 351–359.]

the stars but only once with respect to the Sun, so a Mercury-bound observer would experience alternating years of daylight and darkness.

What if the target is not a sphere but instead is irregular and nonconvex? In this situation, which is most applicable to small asteroids and cometary nuclei, the relationship between the echo power spectrum and

the target's shape is shown in Fig. 7. We must interpret D as the sum of the distances r_+ and r_- from the plane ψ_0 containing the line of sight and the spin vector to the surface elements with the greatest positive (approaching) and negative (receding) line-of-sight velocities. In different words, if the planes ψ_+ and ψ_- are defined as being parallel to ψ_0 and tangent to the target's approaching and receding limbs, then ψ_+ and ψ_- are at distances r_+ and r_- from ψ_0 . Letting f_0 , f_+ , and f_- be the frequencies of echoes from portions of the target intersecting ψ_0 , ψ_+ , and ψ_- , we have $B = f_+ - f_-$. Note that f_0 is the Doppler frequency of hypothetical echoes from the target's center of mass and that any constant-Doppler contour lies in a plane parallel to ψ_0 .

It is useful to imagine looking along the target's pole at the target's projected shape, that is, its pole-on silhouette S . D is simply the width, or "breadth," of this silhouette (or, equivalently, of the silhouette's convex envelope or "hull," H) measured normal to the line of sight (see Fig. 7). In general, r_+ and r_- are

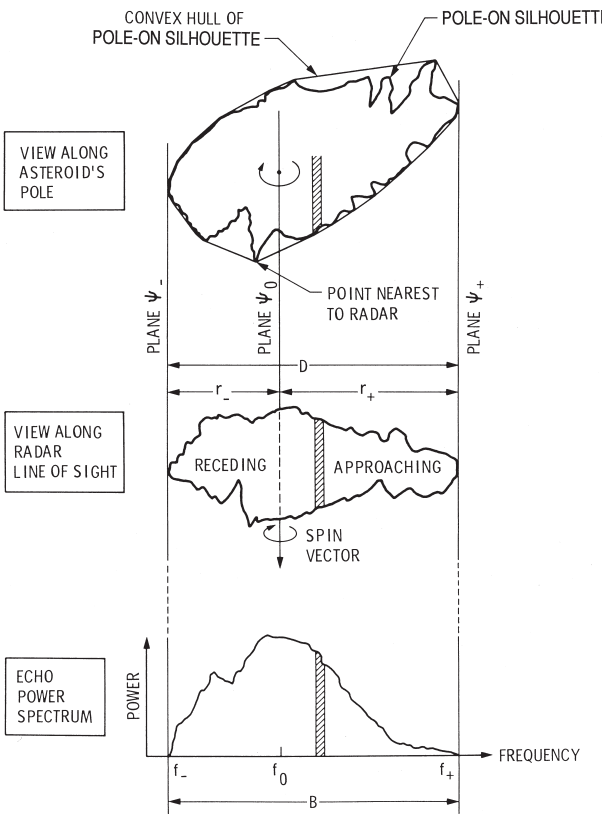


FIGURE 7 Geometric relations between an irregular, nonconvex rotating asteroid and its echo power spectrum. The plane ψ_0 contains the asteroid's spin vector and the asteroid-radar line. The cross-hatched strip of power in the spectrum corresponds to echoes from the cross-hatched strip on the asteroid.

periodic functions of rotation phase ϕ , and depend on the shape of H as well as on the projected location of the target's center of mass, about which H rotates. If the radar data thoroughly sample at least 180° of rotational phase, then in principle one can determine $f_r(\phi)$ and $f_\ell(\phi)$ completely, and can recover H as well as the astrometrically useful quantity f_o . For many small, near-Earth asteroids, pronounced variations in $B(\phi)$ reveal highly noncircular pole-on silhouettes (see Fig. 8 and Section III, J).

D. TOPOGRAPHY ON THE MOON AND INNER PLANETS

For the Moon, Mercury, Mars, and Venus, topography along the subradar track superimposes a modulation on the echo delay above or below that predicted by ephemerides, which generally are calculated for a sphere with the object's a priori mean radius. Prior to spacecraft exploration of these objects, there were radar-detectable errors in the radii estimates as well as in the target's predicted orbit. These circumstances required that an extended series of measurements of the time delay of the echo's leading edge be folded into a computer program designed to estimate simultaneously parameters describing the target's orbit, mean radius, and topography. These programs also contain parameters from models of wave propagation through the interplanetary medium or the solar corona, as well as parameters used to test general relativity, as noted earlier.

Radar has been used to measure topography on the Moon and on the inner planets. For example, Fig. 9 shows a three-dimensional reconstruction of topography derived from altimetric profiles obtained for Mars in the vicinity of the giant shield volcano Arsia Mons. The altimetric resolution of the profiles is about 150 m (1 μ sec in delay), but the surface resolution, or footprint, is very coarse (~ 75 km). Figure 10 shows altitude profiles across impact basins on Mercury. The *Magellan* radar altimeter, with a footprint typically 20 km across and vertical resolution on the order of tens of meters, has produced detailed topographic maps of most of Venus.

E. ANGULAR SCATTERING LAW

The functional forms of the distributions $\sigma(\tau)$ and $\sigma(\nu)$ contain information about the radar scattering process and about the structural characteristics of the target's surface. Suppose the target is a large, smooth, spherical

planet. Then echoes from the subradar region (near the center of the visible disk; see Fig. 5), where the surface elements are nearly perpendicular to the line of sight, would be much stronger than those from the limb regions (near the disk's periphery). This effect is seen visually when one shines a flashlight on a smooth, shiny ball—a bright glint appears where the geometry is right for backscattering. If the ball is roughened, the glint is spread out over a wider area and, in the case of extreme roughness, the scattering would be described as “diffuse” rather than “specular.”

For a specular target, $\sigma(\tau)$ would have a steep leading edge followed by a rapid drop. The power spectrum $\sigma(\nu)$ would be sharply peaked at central frequencies, falling off rapidly toward the spectral edges. If, instead, the spectrum were very broad, severe roughness at some scale(s) comparable to or larger than λ would be indicated. In this case, knowledge of the echo's polarization properties would help to ascertain the particular roughness scale(s) responsible for the absence of the sharply peaked spectral signature of specular scattering.

By inverting the delay or Doppler distribution of echo power, one can estimate the target's average angular scattering law, $\sigma_o(\theta) = d\sigma/dA$, where dA is an element of surface area and θ is the “incidence angle” between the line of sight and the normal to dA . For the portion of the echo's “polarized” (i.e., OC or SL) component that is specularly scattered, $\sigma_o(\theta)$ can be related to statistics describing the probability distribution for the slopes of surface elements. Examples of scattering laws applied in planetary radar astronomy are the Hagfors law,

$$\sigma_o(\theta) \sim C(\cos^4\theta + C \sin^2\theta)^{-3/2} \quad (5)$$

the Gaussian law,

$$\sigma_o(\theta) \sim [C \exp(-C \tan^2\theta)]/\cos^4\theta \quad (6)$$

and the Cosine law,

$$\sigma_o(\theta) \sim (C + 1)\cos^{2C}\theta \quad (7)$$

where $c^{-1/2} = S_o = \langle \tan^2\theta \rangle^{1/2}$ is the adirectional rms slope.

Echoes from the Moon, Mercury, Venus, and Mars are characterized by sharply peaked OC echo spectra (Fig. 11). Although these objects are collectively referred to as “quasi-specular” radar targets, their echoes also contain a diffusely scattered component and have full-disk circular polarization ratios averaging about

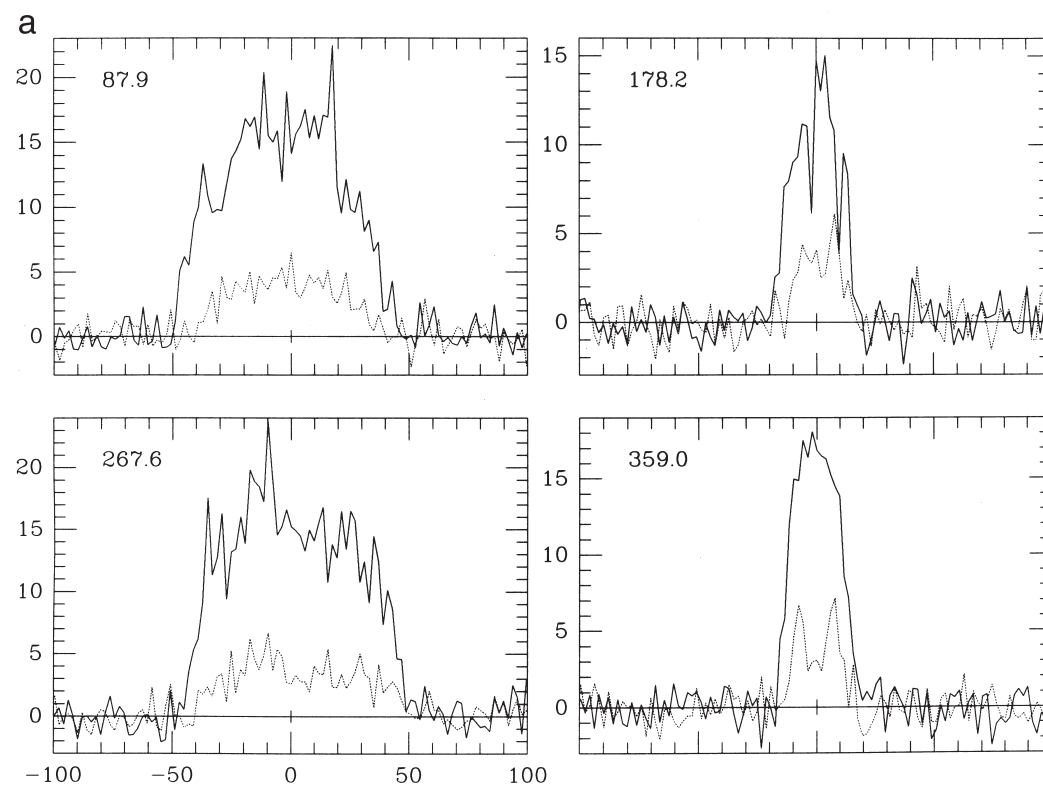


FIGURE 8 Constraints on the shape of near-Earth asteroid 1620 Geographos from Goldstone radar echoes. (a) Spectra obtained at phases of bandwidth extrema. OC (solid curve) and SC (dotted curve) echo power is plotted versus Doppler frequency. (b) Comparison of an estimate of the hull (H) on the asteroid's pole-on silhouette (S) with an estimate of S itself. The white curve is the cw estimate of H and the X marks the projected position of the asteroid's center of mass (COM) with respect to H . That curve and the X are superposed on an estimate of S from delay-Doppler images; the bright pixel is the projection of the COM determined from analysis of those images. The absolute scales and relative rotational orientations of the two figures are known: border ticks are 1 km apart. The offset between the X and the bright pixel is a measure of the uncertainty in our knowledge of the COM's delay-Doppler trajectory during the experiment. In the diagram at right, the arrows point to the observer at phases of lightcurve maxima ($M1$, $M2$) and minima ($m1$, $m2$). [From S. J. Ostro *et al.* (1996). *Icarus* **121**, 46–66.]

0.07 for the Moon, Mercury, and Venus, but ranging from 0.1 to 0.4 for Mars, as discussed next.

Typical rms slopes obtained at decimeter wavelengths for these four quasi-specular targets are around 7° and consequently these objects' surfaces have been described as "gently undulating." As might be expected, values estimated for S_o increase as the observing wavelength decreases. For instance, for the Moon, S_o increases from $\sim 4^\circ$ at 20 m to $\sim 8^\circ$ at 10 cm, to $\sim 33^\circ$ at 1 cm. At optical wavelengths, the Moon shows no trace of a central glint, that is, the scattering is entirely diffuse. This phenomenon arises because the lunar surface (Fig. 12) consists of a regolith (an unconsolidated layer of fine-grained particles) with much intricate structure at the scale of visible wavelengths. At decimeter wavelengths, the ratio of diffusely scattered power to quasi-specularly scattered power is about one-third for the Moon, Mercury, and Venus, but two to three times higher for Mars. This ratio can be determined

by assuming that all the SC echo is diffuse and then calculating the diffusely scattered fraction (x) of OC echo by fitting to the OC spectrum a model based on a "composite" scattering law, for example, $S_o(\theta) = x\sigma_{\text{DIF}}(\theta) + (1 - x)\sigma_{\text{QS}}(\theta)$. Here $\sigma_{\text{QS}}(\theta)$ might be the Hagfors law and usually $\sigma_{\text{DIF}}(\theta) \sim \cos^m \theta$; when this is done, estimated values of m usually fall between unity (geometric scattering, which describes the optical appearance of the full Moon) and two (Lambert scattering).

For the large, nearly spherical asteroids 1 Ceres and 2 Pallas (see Section III, J), the closeness of μ_c to zero indicates quasi-specular scattering, but the OC spectra, rather than being sharply peaked, are fit quite well using a Cosine law with C between 2 and 3, or a Gaussian law with C between 3 and 5. Here we can safely interpret the diffuse echo as due to the distribution of surface slopes, with S_o between 20° and 50° . OC echo spectra obtained from asteroid 4 Vesta and

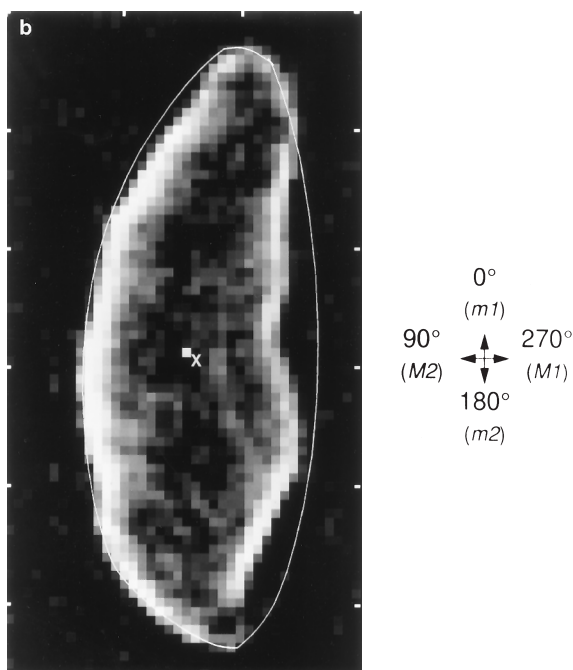


FIGURE 8 (continued)

Jupiter's satellite Io have similar shapes, but these objects' substantial polarization ratios ($\mu_c \sim 0.3$ and ~ 0.5 , respectively) suggest that small-scale roughness is at least partially responsible for the diffuse echoes. Circular polarization ratios between 0.5 and 1.0 have been measured for several asteroids (see Table II) and parts of Mars and Venus, implying extreme decimeter-scale roughness, perhaps analogous to terrestrial lava flows (Fig. 13). Physical interpretations of the diffusely scattered echo employ information about albedo, scattering law, and polarization to constrain the size distributions, spatial densities, and electrical properties of wavelength-scale rocks near the surface, occasionally using the same theory of multiple light scattering applied to radiative transfer problems in other astrophysical contexts.

F. RADAR MAPPING OF SPHERICAL TARGETS

The term "radar image" usually refers to a measured distribution of echo power in delay, Doppler, and/or up to two angular coordinates. The term "radar map" usually refers to a display in suitable target-centered coordinates of the residuals with respect to a model that parameterizes the target's size, shape, rotation, average scattering properties, and possibly its motion

with respect to the delay-Doppler ephemerides. Knowledge of the dimensions of the Moon and inner planets has long permitted conversion of radar images to maps of these targets. For small asteroids, the primary use of images is to constrain the target's shape (see Section III, J).

As illustrated in Fig. 5, intersections between constant-delay contours and constant-Doppler contours on a sphere constitute a "two-to-one" transformation from the target's surface to delay-Doppler space. For any point in the northern hemisphere, there is a conjugate point in the southern hemisphere at the same delay and Doppler. Therefore, the source of echo in any delay-Doppler resolution cell can be located only to within a twofold ambiguity. This north-south ambiguity can be avoided completely if the radar beamwidth (~ 2 arcmin for Arecibo at 13 cm or Goldstone at 3.5 cm) is comparable to or smaller than the target's apparent angular radius, as in the case of observations of the Moon (angular radius ~ 15 arcmin). Similarly, no such ambiguity arises in the case of side-looking radar observations from spacecraft (e.g., the *Magellan* radar) for which the geometry of delay-Doppler surface contours differs somewhat from that in Fig. 5. For ground-based observations of Venus and Mercury, whose angular radii never exceed a few tens of arcseconds, the separation of conjugate points is achievable by either (1) offsetting the pointing to place a null of the illumination pattern on the undesired hemisphere or (2) interferometrically, using two receiving antennas, as follows.

The echo waveform received at either antenna from one conjugate point will be highly correlated with the echo waveform received at the other antenna from the same conjugate point. However, echo waveforms from the two conjugate points will be largely uncorrelated with each other, no matter where they are received. Thus, echoes from two conjugate points can, in principle, be distinguished by cross-correlating echoes received at the two antennas with themselves and with each other, and performing algebraic manipulations on long time averages of the cross product and the two self products.

The echo waveform from a single conjugate point will experience slightly different delays in reaching the two antennas, so there will be a phase difference between the two received signals, and this phase difference will depend only on the geometrical positions of the antennas and the target. This geometry will change as the Earth rotates, but very slowly and in a predictable manner. The antennas are best positioned so contours of constant phase difference on the target disk are as orthogonal as possible to the constant-Doppler con-

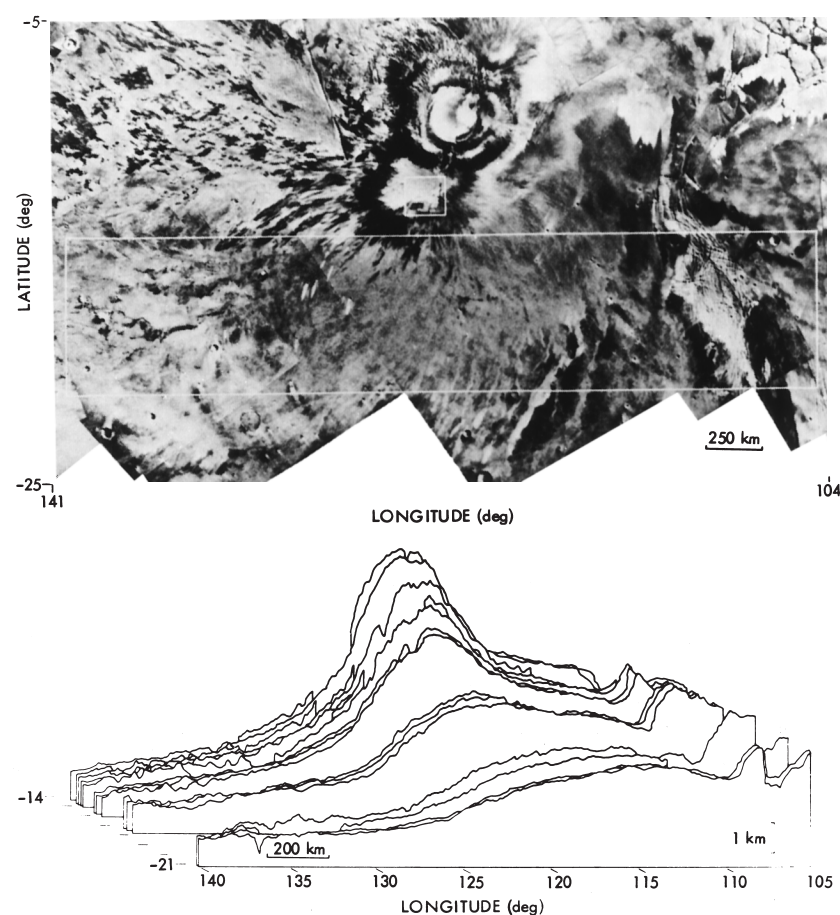


FIGURE 9 Topographic contours for the southern flank (large rectangle) of the Martian shield volcano Arsia Mons, obtained from radar altimetry. [From L. Roth, G. S. Downs, R. S. Saunders, and G. Schubert (1980). *Icarus* 42, 287–316.]

tours, which connect conjugate points. Phase difference hence becomes a measure of north–south position, and echoes from conjugate points can be distinguished on the basis of their phase relation.

The total number of “fringes,” or cycles of phase shift, spanned by the disk of a planet with diameter D and a distance R from the radar is approximately $(D/R)(b_{\text{proj}}/\lambda)$, where b_{proj} is the projection of the interferometer baseline normal to the mean line of sight. For example, Arecibo interferometry linked the main antenna to a 30.5-m antenna about 11 km farther north. It placed about seven fringes on Venus, quite adequate for separation of the north–south ambiguity. The Goldstone main antenna (see Fig. 3) has been linked to smaller antennas to perform three-element as well as two-element interferometry. Tristatic observations permit one to solve so precisely for the north–south location of a given conjugate region that one can obtain the region’s elevation relative to the mean

planetary radius. Altimetric information can be extracted also from bistatic observations using the time history of the phase information, but only if the variations in the projected baseline vector are large enough.

In constructing a radar map, the unambiguous delay-Doppler distribution of echo power is transformed to planetocentric coordinates, and a model is fit to the data, using a maximum-likelihood or weighted-least-squares estimator. The model contains parameters for quasi-specular and diffuse scattering as well as prior information about the target’s dimensions and spin vector. For Venus, effects of the dense atmosphere on radar wave propagation must also be modeled. Residuals between the data and the best-fit model constitute a radar reflectivity map of the planet. Variations in radar reflectivities evident in radar maps can be caused by many different physical phenomena, and their proper interpretation demands due attention to the radar wavelength, echo polarization, viewing geome-

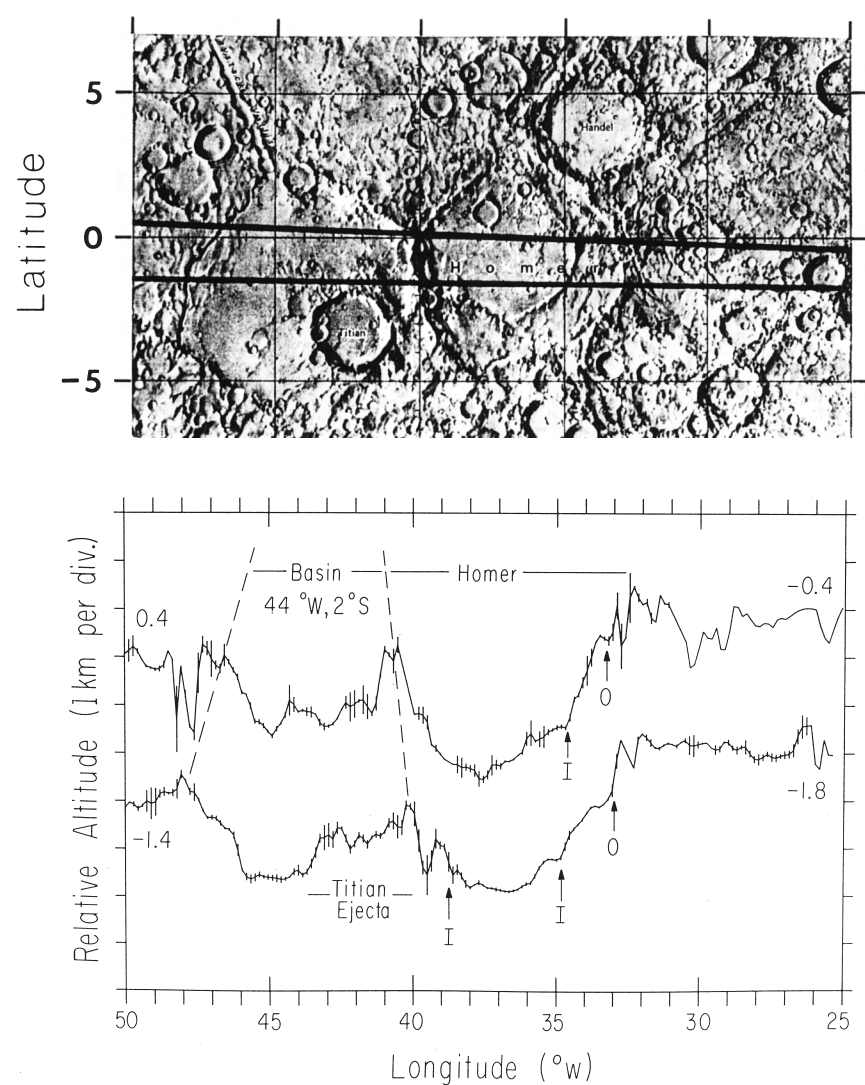


FIGURE 10 Mercury altitude profiles (bottom) showing topography across Homer Basin and a large, unnamed basin to the west, estimated from observations whose subradar tracks are shown on the USGS shaded-relief map (top). Broken lines indicate approximate locations of the basin rims as seen in *Mariner 10* images. Arrows locate Homer's inner/outer (I/O) basin rings. [From J. K. Harmon, D. B. Campbell, D. L. Bindshadler, J. W. Head, and I. I. Shaprio (1986). *J. Geophys. Res.* **91**, 385–401.]

try, prior knowledge about surface properties, and the nature of the target's mean scattering behavior. Similar considerations apply to inferences based on disk-integrated radar albedos.

Delay-Doppler interferometry is not currently feasible for targets like the Galilean satellites and the largest asteroids, which are low-SNR and overspread (see Section II, D). A different, "Doppler mapping" technique, developed for these spherical targets, reconstructs the global albedo distribution from cw echo spectra acquired as a function of rotation phase and at an arbitrary number of subradar latitudes. To visualize

how Doppler mapping works, note that a target's reflectivity distribution can be expanded as a truncated spherical harmonic series, and that the distribution of echo power in rotation phase and Doppler frequency can be obtained as a linear, analytic function of the series coefficients. Estimation of those coefficients from an observed phase-Doppler distribution can be cast as a least-squares problem to form a linear imaging system. Doppler mapping works best when the limb-darkening is minimal and is ideally suited to overspread targets whose echoes are too weak for the random-code method. Removal of the north-south ambiguity

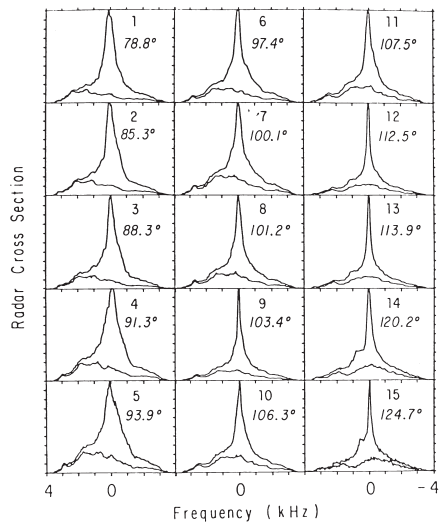


FIGURE 11 Mars 13-cm radar echo spectra for subradar points along 22° north latitude at the indicated west longitudes, obtained in the OC (upper curves) and SC (lower curves) polarizations. In each box, spectra are normalized to the peak OC cross section. The echo bandwidth is 7.1 kHz. Very rough regions on the planet are revealed as bumps in the SC spectra, which move from positive to negative Doppler frequencies as Mars rotates. [From J. K. Harmon, D. B. Campbell, and S. J. Ostro (1982). *Icarus* **52**, 171–187.]

in Doppler images (or in single-antenna delay-Doppler images) is possible if the data sample nonequatorial subradar latitudes, because then the Doppler (or delay-Doppler) versus rotation-phase trajectories of conjugate points are different.

Recently, a new kind of radar observation using Goldstone as a 3.5-cm cw transmitter and the Very Large Array in New Mexico as a synthetic aperture receiver has been used for direct measurement of the angular distribution of echo power. The 27-antenna VLA constitutes a 351-baseline interferometer whose synthesized beamwidth is as narrow as 0.24 arcsec at the Goldstone transmitter frequency, providing resolutions of roughly 80, 40, and 70 km for Mercury, Venus, and Mars at closest approach. (The finest resolutions in published ground-based delay-Doppler maps of those planets are approximately 15, 1, and 40 km, but the maps cover small fractions of the surface at such fine resolutions.) Radar aperture synthesis has produced full-disk images of those planets and Saturn's rings that are free from north–south ambiguities, avoid problems related to overspreading, and permit direct measurement of local albedo, polarization ratio, and scattering law. The Goldstone–VLA system has achieved marginal angular resolution of main belt asteroid echoes and could readily image any large-particle comet clouds as radar detectable as the one around

comet IRAS-Araki-Alcock. Goldstone–VLA resolution of asteroids and comet nuclei is impaired by the VLA's coarse spectral resolution (>380 Hz) and inability to accommodate time-modulated waveforms. Figures 14–18 show examples of radar maps constructed using various techniques.

G. RADAR EVIDENCE FOR ICE DEPOSITS AT MERCURY'S POLES

The first full-disk (Goldstone–VLA) radar portraits of Mercury surprisingly revealed anomalously bright polar features with $\mu_c > 1$, and subsequent delay-Doppler imagery from Arecibo established that the anomalous radar echoes originate from interiors of craters that are perpetually shaded from sunlight because of Mercury's near-zero obliquity (see Fig. 15). The angle between the orbital planes of Mercury and Earth is 7°, so portions of the permanently shadowed regions are visible to Earth-based radars. Most of the south pole anomalies are confined to the floor of the 155-km crater Chao Meng-Fu. At each pole, bright radar features in regions imaged by *Mariner 10* correlate exactly with craters; numerous radar features lie in the hemisphere not imaged by that spacecraft.

Similarities between the radar scattering properties of the Mars and Mercury polar anomalies and those of the icy Galilean satellites (see Section III, K) support the inference that the radar anomalies are deposits of water ice. Temperatures below 120 K in the permanent shadows are expected and are low enough for ice to be stable against sublimation for billions of years. Temperatures several tens of kelvins lower may exist inside high-latitude craters and perhaps also beneath at least 10 cm of optically bright regolith. Plausible sources of water on Mercury include comet impacts and outgassing from the interior. It has been noted that most water vapor near the surface is photodissociated, but that some molecules will random-walk to polar cold traps. Ices of other volatiles, including CO₂, NH₃, HCN, and SO₂, might also be present.

H. VENUS REVEALED BY *MAGELLAN*

The *Magellan* spacecraft entered Venus orbit in August 1990 and during the next two years explored the planet with a single scientific instrument operating as a radar imager, an altimeter, and a thermal radiometer. *Magellan's* imaging resolution (~ 100 m) and altimetric resolution (5 to 100 m) improves upon the best previous spacecraft and ground-based measurements by an



FIGURE 12 Structure on the lunar surface near the *Apollo 17* landing site. Most of the surface is smooth and gently undulating at scales much larger than a centimeter. This smooth component of the surface is responsible for the predominantly quasi-specular character of the Moon’s radar echo at $\lambda \gg 1$ cm. Wavelength-scale structure produces a diffuse contribution to the echo. Wavelength-sized rocks are much more abundant at $\lambda \sim 4$ cm than at $\lambda \sim 10$ m (the scale of the boulder being inspected by astronaut H. Schmitt), and hence diffuse echo is more substantial at shorter wavelengths.



FIGURE 13 This lava flow near Sunset Crater in Arizona is an example of an extremely rough surface at decimeter scales and is similar to terrestrial flows yielding large circular polarization ratios at decimeter wavelengths.

order of magnitude, and does so with nearly global coverage. Analysis of *Magellan*’s detailed, comprehensive radar reconnaissance of Venus’s surface topography, morphology, and electrical properties ultimately will revolutionize our understanding not only of that planet, but of planetary geology itself.

Venus’s surface contains a plethora of diverse tectonic and impact features, but its formation and evolution have clearly been dominated by widespread volcanism, whose legacy includes pervasive volcanic planes, thousands of tiny shield volcanoes, monoumental edifices, sinuous lava flow channels, pyroclastic deposits, and pancakelike domes. The superposition of volcanic signatures and elaborate, complex tectonic forms records a history of episodic crustal deformation. The paucity of impact craters smaller than 25 km and the lack of any as small as a few kilometers attests to the protective effect of the dense atmosphere. The multilobed, asymmetrical appearance of many large craters presumably results from atmospheric breakup of projectiles before impact. Atmospheric entrainment and transport of ejecta are evident in very elongated

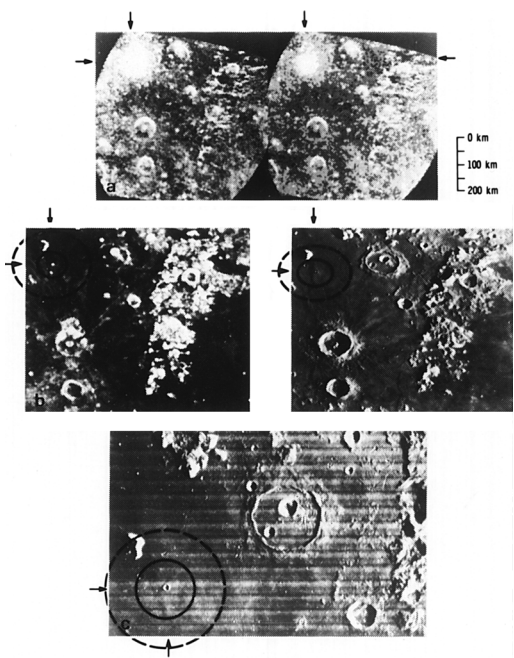


FIGURE 14 The lunar crater Piton B (located by arrows) is surrounded by an ejecta blanket that is conspicuous in the 3.8-cm-radar image (displayed in both continuous- and incremental-tone maps) but invisible in Earth-based and Lunar Orbiter photographs. The sketched 50- and 100-km-diameter circles are concentric to the crater and coplanar with the local mean surface. (Courtesy of T. W. Thompson.)

ejecta blankets. Numerous craters are surrounded by radar-dark zones, perhaps the outcome of atmospheric pressure-wave pulverization and elevation of surface material that upon resettling deposited a tenuous and hence unreflective “impact regolith.” Figure 17 shows examples of *Magellan* radar images.

I. THE RADAR HETEROGENEITY OF MARS

Ground-based investigations of Mars have achieved more global coverage than those of the other terrestrial targets, because the motion in longitude of the subradar point on Mars (whose rotation period is only 24.6 hr) is rapid compared to that on the Moon, Venus, or Mercury, and because the geometry of Mars’s orbit and spin vector permits subradar tracks throughout the Martian tropics. The existing body of Mars radar data reveals extraordinary diversity in the degree of small-scale roughness as well as in the rms slope of smooth surface elements. For example, Fig. 19 shows the variation in OC echo spectral shape as a function of longitude for a subradar track along ~16°S latitude. Slopes on Mars have rms values from less than 0.5° to more than 10°. Chryse Planitia, site of the first Viking Lander, has fairly shallow slopes (4°–5°) and, in fact, radar rms slope estimates were utilized in selection of the Viking Lander (and Mars Pathfinder) sites.

Diffuse scattering from Mars is much more substan-

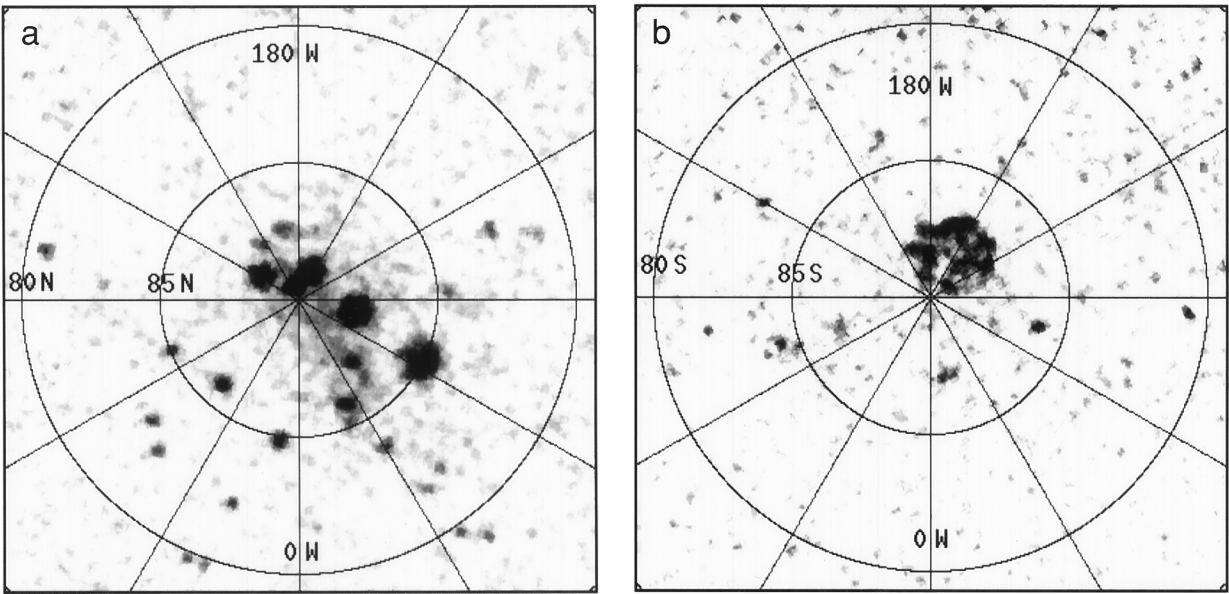


FIGURE 15 Arecibo 13-cm delay-Doppler images of the (a) north and (b) south poles of Mercury, taken in the SC polarization. The resolution is 15 km. The radar-brightness regions are shown here as dark. [From J. K. Harmon, M. A. Slade, R. A. Velez, A. Crespo, M. J. Dryer, and J. M. Johnson (1994). *Nature* **369**, 213–215. Copyright 1994 Macmillan Magazines Limited.]

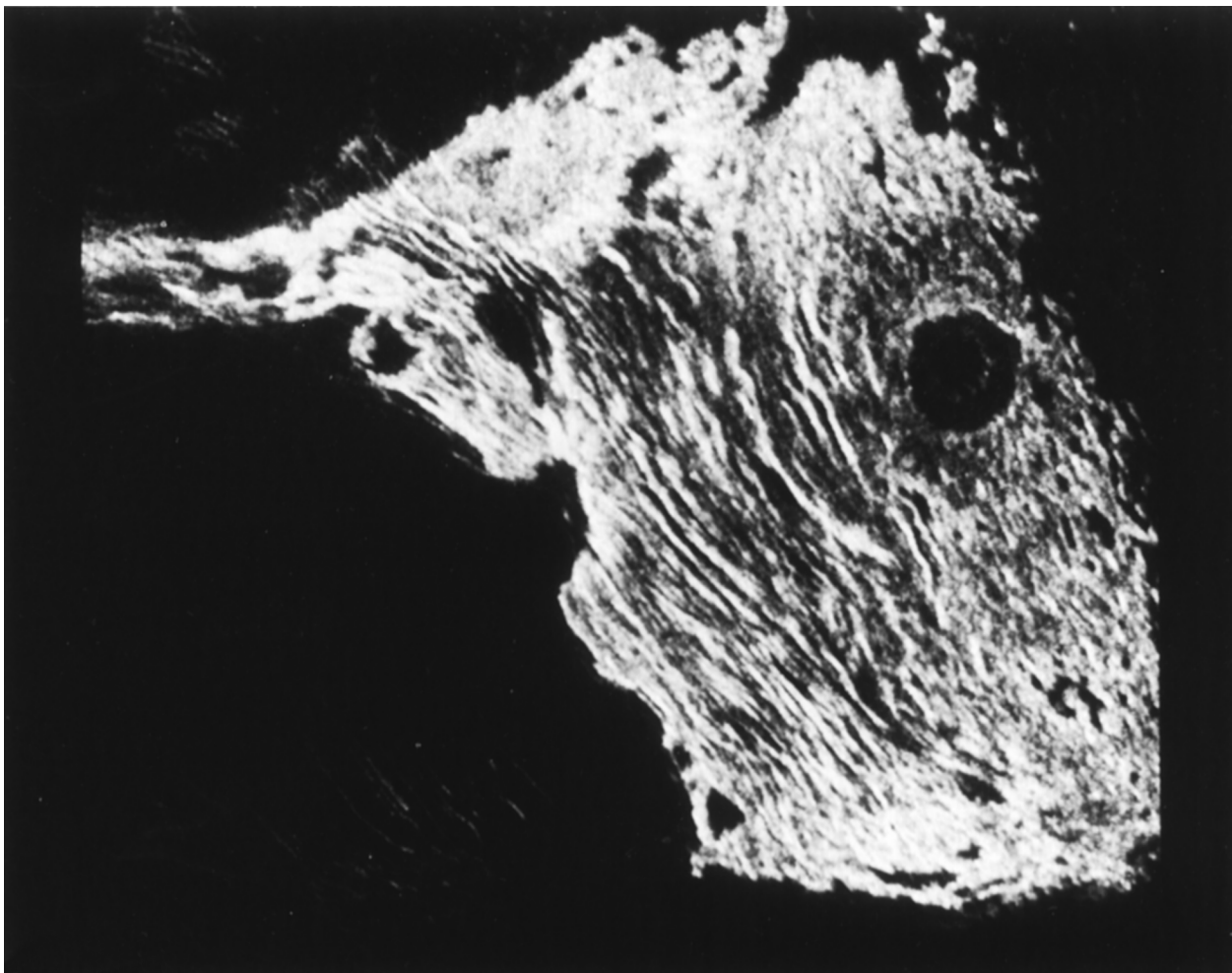


FIGURE 16 Arecibo delay-Doppler OC radar map of Maxwell Montes on Venus. (Courtesy of D. B. Campbell.)

tial than for the other quasi-specular targets, and often accounts for most of the echo power, so the average near-surface abundance of centimeter-to-meter-scale rocks presumably is much greater on Mars than on the Moon, Mercury, or Venus. Features in Mars SC spectra first revealed the existence of regions of extremely small-scale roughness (see Fig. 11), and the trajectory of these features' Doppler positions versus rotation phase suggested that their primary sources are the Tharsis and Elysium volcanic regions. The best terrestrial analog for this extremely rough terrain might be young lava flows (see Fig. 13). Goldstone-VLA images of Mars at longitudes that cover the Tharsis volcanic region (see Fig. 18) confirm that this

area is the predominant source of strong SC echoes and that localized features are associated with individual volcanoes. A 2000-km-long band with an extremely low albedo cuts across Tharsis; the radar darkness of this "Stealth" feature probably arises from an underdense, unconsolidated blanket of pyroclastic deposits ~ 1 m deep. The strongest SC feature in the Goldstone-VLA images is the residual south polar ice cap, whose scattering behavior is similar to that of the icy Galilean satellites (Section III, K). Arecibo observations of Mars, including Doppler-only and random-code delay-Doppler mapping, have charted the detailed locations and fine structure of Mars SC features (see Fig. 18b).

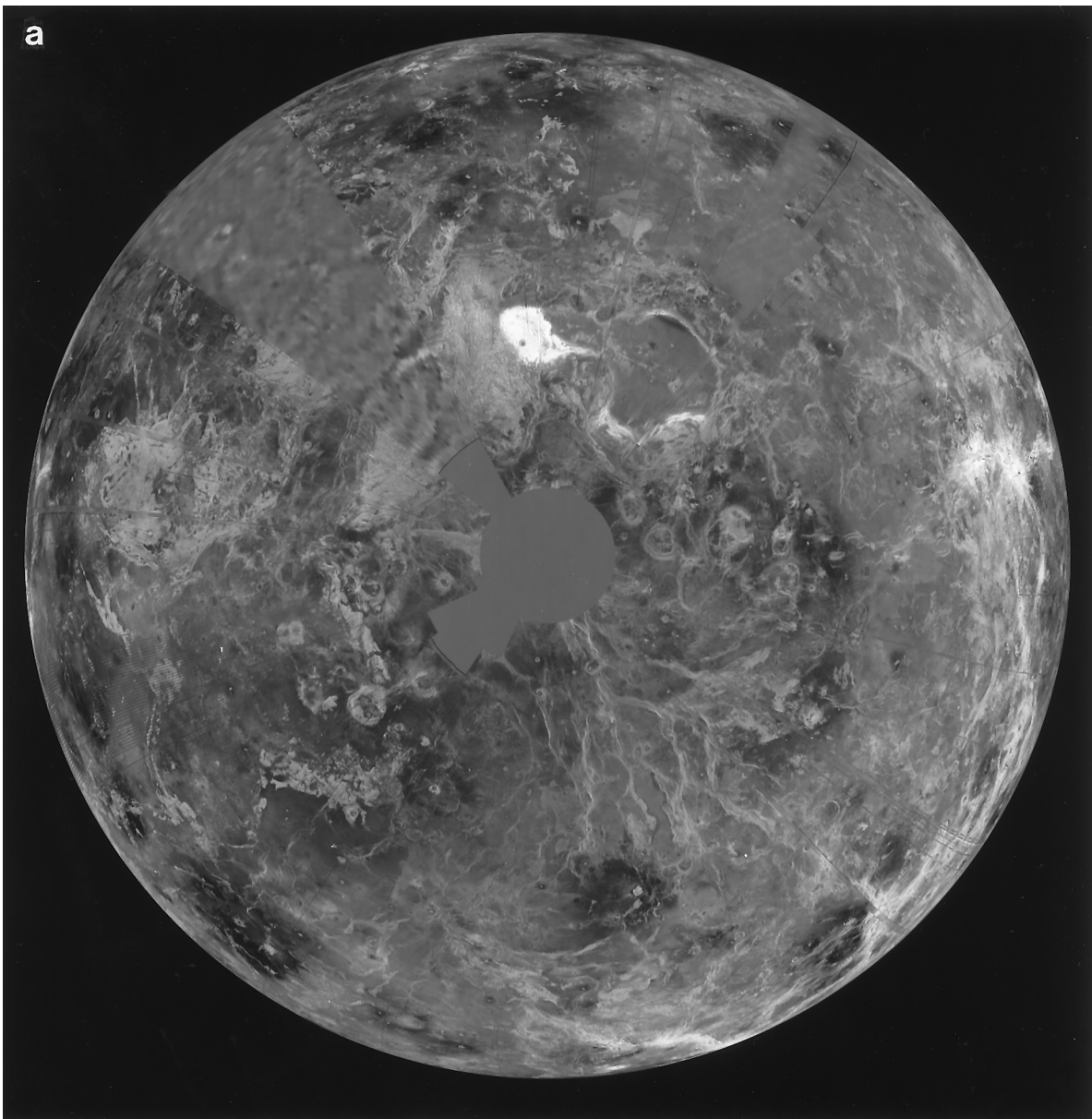


FIGURE 17 *Magellan* radar maps of Venus. (a) Northern-hemisphere projection of mosaics. The north pole is at the center of the image, with 0° and 90°E longitudes at the six and three o'clock positions. Gaps use Pioneer Venus data or interpolations. The bright, porkchop-shaped feature is Maxwell Montes, a tectonically produced mountain range first seen in ground-based images. (b) 120-m-resolution map of the crater Cleopatra on the eastern slopes of Maxwell Montes. Cleopatra is a double-ringed impact basin that resembles such features seen on the Moon, Mercury, and Mars. (Courtesy of JPL/NASA.)

J. ASTEROIDS

Echoes from 37 main belt asteroids (MBAs) and 47 near-Earth asteroids (NEAs) have provided a wealth of new information about these objects' sizes, shapes, spin vectors, and surface characteristics such as decimeter-scale morphology, topographic relief, regolith porosity, and metal concentration. During the past de-

cade, radar has been established as the most powerful Earth-based technique for determining the physical properties of asteroids that come close enough to yield strong echoes.

The polarization signatures of some of the largest MBAs (e.g., 1 Ceres and 2 Pallas) reveal surfaces that are smoother than that of the Moon at decimeter scales but much rougher at some much larger scale. For ex-

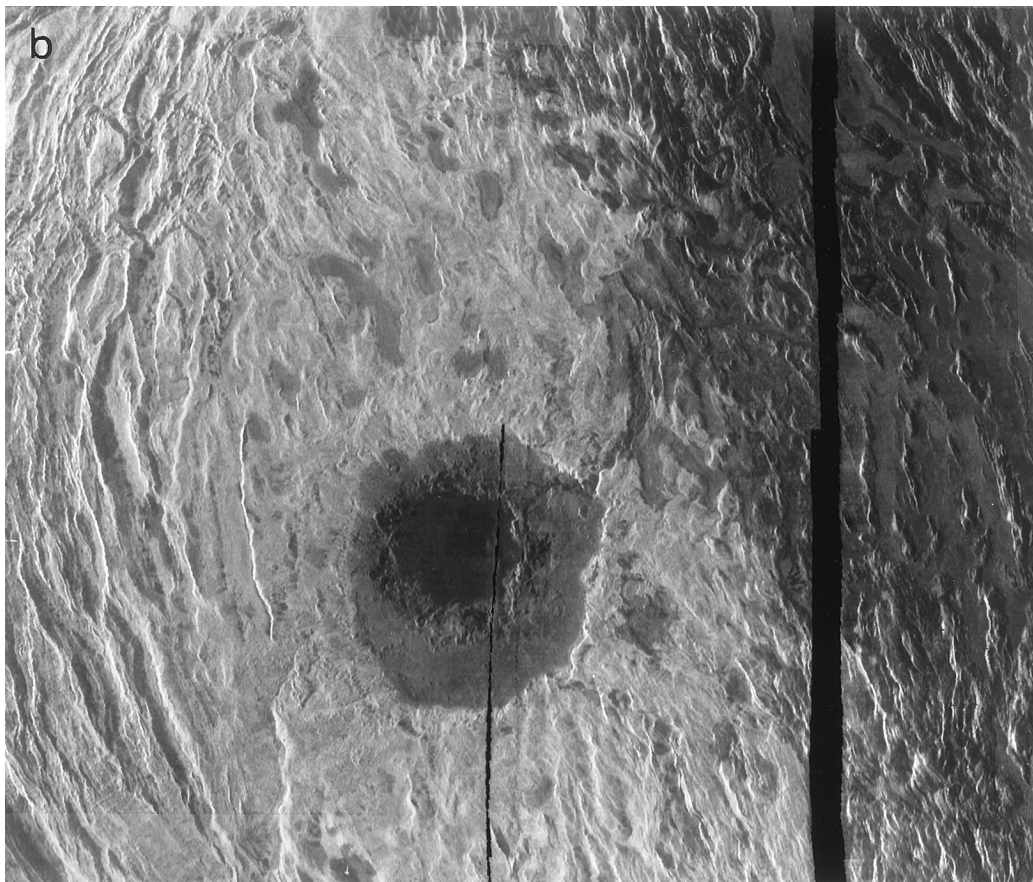


FIGURE 17 (continued)

ample, for Pallas, μ_c is only ~ 0.05 and, as noted earlier, surface slopes exceed 20° . For asteroids in the 200-km-diameter range, the echoes provide evidence for large-scale topographic irregularities. For example, brightness spikes within narrow ranges of rotation phase suggest large, flat regions on 7 Iris (Fig. 20), 9 Metis, and 654 Zelinda, whereas bimodal spectra imply nonconvex, possibly bifurcated shapes for 12 Victoria and 216 Kleopatra.

There is a 10-fold variation in the radar albedos of MBAs, implying substantial variations in these objects' surface porosities or metal concentrations, or both. The lowest MBA albedo estimate, 0.04 for Ceres, indicates a lower surface bulk density than that on the Moon. The highest MBA albedo estimates, 0.31 for 16 Psyche and 0.44 for Kleopatra, are consistent with metal concentrations near unity and lunar porosities. These objects might be the collisionally stripped cores of differentiated asteroids and by far the largest pieces of refined metal in the solar system.

The diversity of NEA radar signatures is extreme (see Table II). Some small NEAs are much rougher at

decimeter scales than MBAs, comets, or the terrestrial planets. The radar albedo of the 2-km object 6178 (1986DA), 0.58, strongly suggests that this Earth-approacher is a regolith-free metallic fragment, presumably derived from the interior of a much larger object that melted, differentiated, cooled, and subsequently was disrupted in a catastrophic collision. This asteroid, which appears extremely irregular at 10- to 100-m scales and shows hints of being bifurcated, might be (or have been a part of) the parent body of some iron meteorites. At the other extreme, an interval estimate for 1986JK's radar albedo (0.005 to 0.07) suggests a surface bulk density within a factor of 2 of 0.9 g cm^{-3} . Similarly, the distribution of NEA circular polarization ratios runs from near zero to near unity. The highest values, for 2101 Adonis, 1992QN, 3103 Eger, and 3980 1980PA, indicate extreme near-surface structural complexity, but we cannot distinguish between multiple scattering from subsurface heterogeneities (see Section III, K) and single scattering from complex structure on the surface.

The MBAs 951 Gaspra and 243 Ida, imaged by the

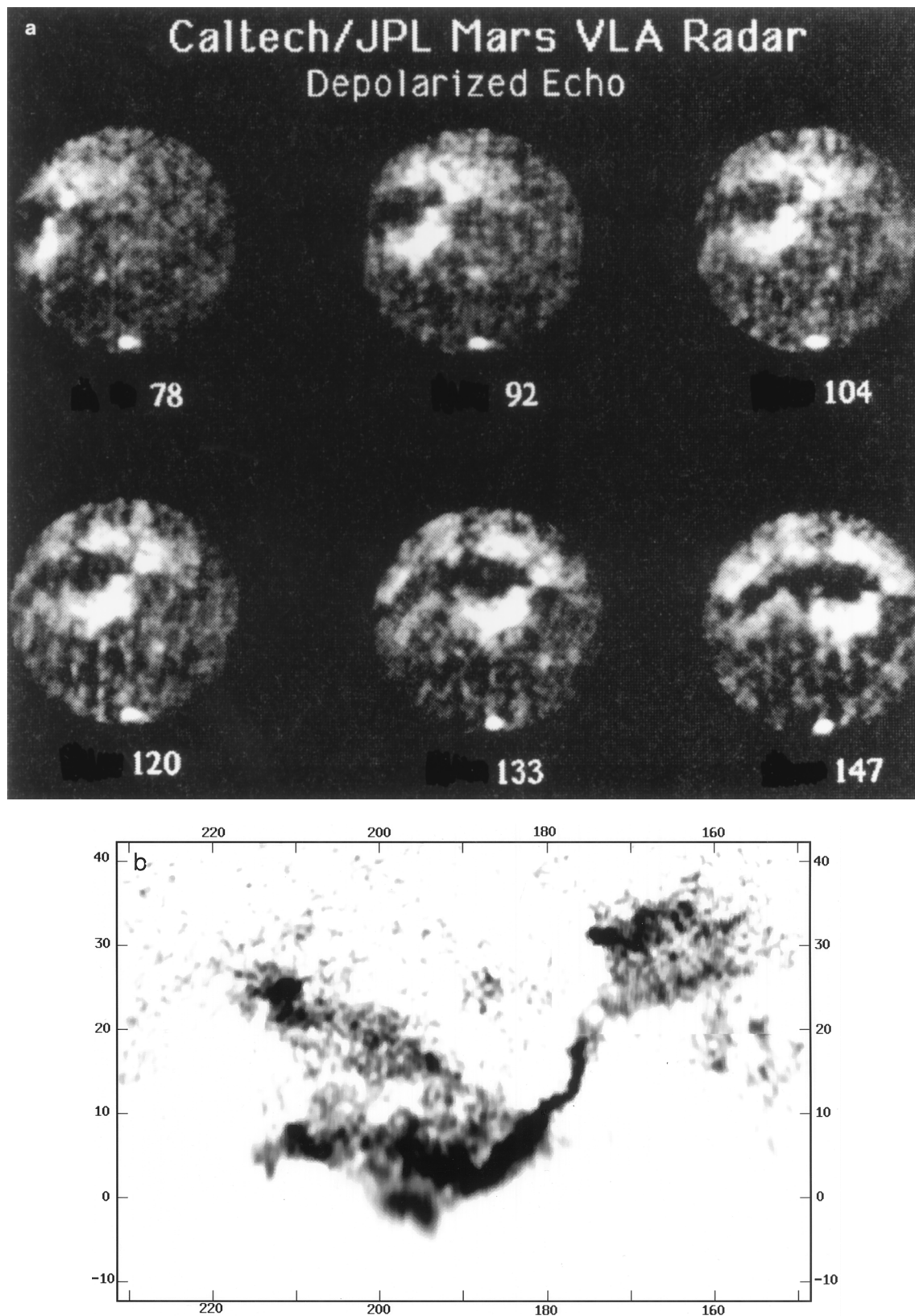


FIGURE 18 Mars radar maps. (a) Goldstone–VLA 3.5-cm, SC radar images of Mars at six longitudes. In the northern hemisphere, the brightest features are in Tharsis, which is traversed by the low-albedo Stealth region. Note the very bright residual south polar ice cap. [From D. O. Muhleman, B. J. Butler, A. W. Grossman, and M. A. Slade (1991). *Science* **253**, 1508–1513. Copyright 1991 American Association for the Advancement of Science.] (b) Arecibo 13-cm, SC reflectivity map of the Elysium region of Mars, obtained from random-code observations made with the subradar latitude 10°S. The map is north–south ambiguous, but more northerly observations confirm that all of the strong features come from the north. The radar-bright regions (shown here as dark) correspond to Elysium Mons (at ~214°W longitude, 25°N latitude) and the Elysium flood basin and outflow channel. The SC brightness of these regions is probably caused by extremely rough lava flows. [From J. K. Harmon, M. P. Sulzer, P. J. Perillat, and J. F. Chandler (1992). *Icarus* **95**, 153–156.]

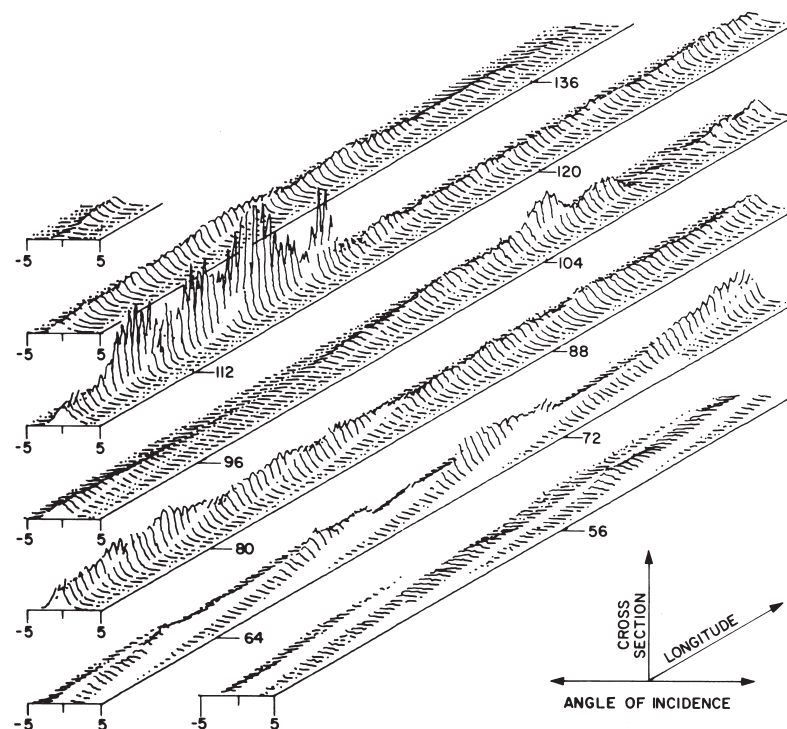


FIGURE 19 Mars echo power spectra as a function of longitude obtained along a subradar track at 16° south latitude. The most sharply peaked spectra correspond to the smoothest regions (i.e., the smallest rms slopes). (Courtesy of G. S. Downs, P. E. Reichley, and R. R. Green.)

Galileo spacecraft, probably are marginally detectable with the upgraded Arecibo. Both Goldstone and Arecibo have investigated the Gaspra-sized Martian moon Phobos, whose radar properties differ from those of most small, Earth-approaching objects but resemble those of large (~ 100 -km), C-class, main belt asteroids. Phobos's surface characteristics may be more representative of Ceres and Pallas than most NEAs. The upper limit on the radar cross section of Deimos, which has defied radar detection, argues for a surface bulk density no greater than about 1 g cm^{-3} .

During the past decade, delay-Doppler imaging of asteroids has produced spatial resolutions as fine as a few decameters. The images generally can be "north-south" ambiguous, that is, they constitute a two-to-one (or even many-to-one) mapping from the surface to the image. However, if the radar is not in the target's equatorial plane, then the delay-Doppler trajectory of any surface point is unique. Hence images that provide adequate orientational coverage can be inverted, and in principle one can reconstruct the target's three-dimensional shape as well as its spin state, the radar-scattering properties of the surface, and the motion of the center of mass through the delay-Doppler ephemerides.

The first asteroid radar data set suitable for recon-

struction of the target's shape was a 2.5-hr sequence of 64 delay-Doppler images of 4769 Castalia (1989PB) (Fig. 21a), obtained two weeks after its August 1989 discovery. The images, which were taken at a subradar latitude of about 35° , show a bimodal distribution of echo power over the full range of sampled rotation phases, and least-squares estimation of Castalia's three-dimensional shape (Fig. 21b) reveals it to consist of two kilometer-sized lobes in contact. Castalia apparently is a contact-binary asteroid formed from a gentle collision of the two lobes.

If the radar view is equatorial, unique reconstruction the asteroid's three-dimensional shape is ruled out, but a sequence of images that thoroughly samples rotation phase can allow unambiguous reconstruction of the asteroid's pole-on silhouette. For example, observations of 1620 Geographos yield ~ 400 images with ~ 100 -m resolution. The pole-on silhouette's extreme dimensions are in a ratio, 2.76 ± 0.21 , that establishes Geographos as the most elongated solar system object imaged so far (see Fig. 8). The images show craters as well as indications of other sorts of large-scale topographic relief, including a prominent central indentation. Protuberances at the asteroid's ends may be related to the pattern of ejecta removal and deposition caused by the asteroid's gravity field.

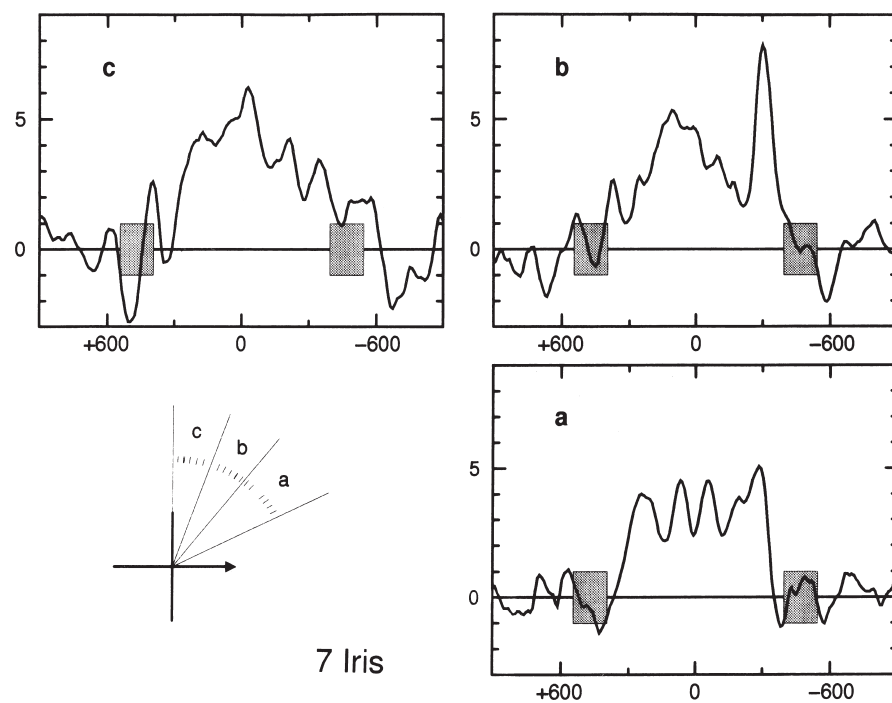


FIGURE 20 Thirteen-centimeter echo spectra of the ~ 200 -km-diameter asteroid 7 Iris, obtained within three narrow rotation-phase intervals. OC echo power in standard deviations is plotted versus Doppler frequency. The shaded boxes show frequency intervals thought to contain the echo edges. A radar “spike” appears in (b) at -305 Hz, but not in spectra at adjacent phases, so it is probably not due to a reflectivity feature but rather to a temporary surge in radar-facing surface area, perhaps a flat facet ~ 20 km wide. [From D. L. Mitchell *et al.* (1995). *Icarus* **118**, 105–131.]

Delay-Doppler imaging of 4179 Toutatis in December 1992 achieved resolutions as fine as 125 nsec (19 m in range) and 8.3 mHz (0.15 mm sec^{-1} in radial velocity), placing hundreds to thousands of pixels on the asteroid. This data set provides physical and dynamical information that is unprecedented for an Earth-crossing object. The images (Fig. 22) reveal this asteroid to be in a highly unusual, non-principal-axis (NPA) spin state with several-day characteristic time-scales. Extraction of the information in this imaging data set required inversion with a much more comprehensive physical model than in the analysis of Castalia images; free parameters included the asteroid’s shape and inertia matrix, initial conditions for the asteroid’s spin and orientation, the radar scattering properties of the surface, and the delay-Doppler trajectory of the center of mass. The shape (Fig. 23) reconstructed from the low-resolution images of Toutatis has shallow craters, linear ridges, and a deep topographic “neck” whose geologic origin is not known. It may have been sculpted by impacts into a single, coherent body, or Toutatis might actually consist of two separate objects that came together in a gentle collision. Toutatis is rotating in a long-axis mode (see Fig. 23) characterized

by periods of 5.4 days (rotation about the long axis) and 7.4 days (average for long-axis precession about the angular momentum vector). The asteroid’s principal moments of inertia are in ratios within 1% of 3.22 and 3.09, and the inertia matrix is indistinguishable from that of a homogeneous body. Such information has yet to be determined for any other asteroid or comet, and probably is impossible to acquire in a fast spacecraft flyby. Higher-resolution images (e.g., Fig. 22b) from the 1992 and 1996 experiments are now being used to refine the Toutatis model.

Accurate shape models of near-Earth asteroids open the door to a wide variety of theoretical investigations that previously have been impossible or have used simplistic models (spheres or ellipsoids). For example, the Castalia and Toutatis models are being used to explore the stability and evolution of close orbits, with direct application to the design of robotic and piloted spacecraft missions, to studies of retention and redistribution of impact ejecta, and to questions about plausible origins and lifetimes of asteroidal satellites. Accurate models also allow realistic investigations of the effects of collisions in various energy regimes on the object’s rotation state, surface topography, regolith, and inter-

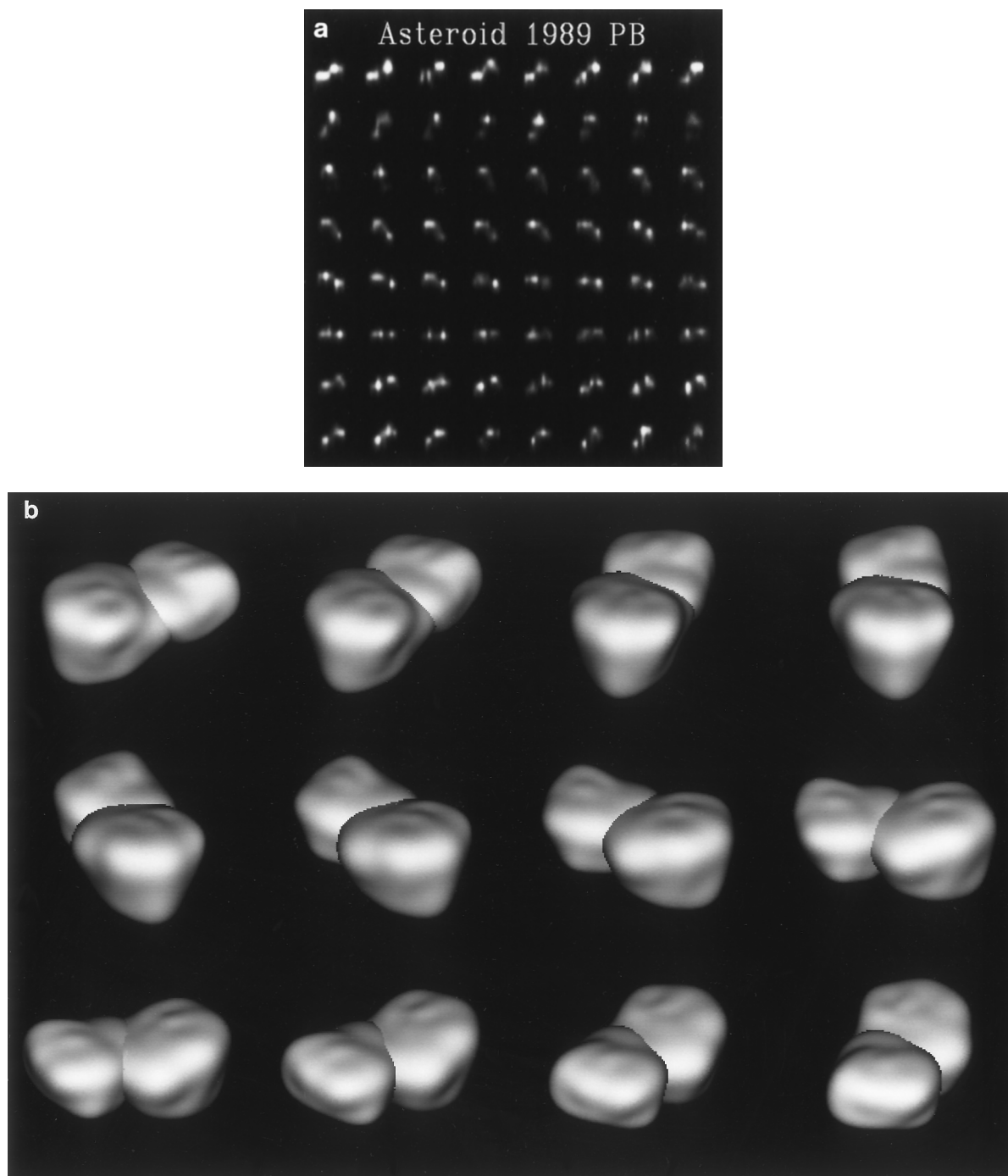


FIGURE 21 Radar results for near-Earth asteroid 4769 Castalia (1989PB). (a) Arecibo radar images. This 64-frame “movie” is to be read like a book (left to right in the top row, etc.). The radar lies toward the top of the page, in the image plane, which probably is about 35° from the asteroid’s equatorial plane. In each frame, OC echo power (i.e., the brightness seen by the radar) is plotted versus time delay (increasing from top to bottom) and frequency (increasing from left to right). The object is seen rotating through about 220° during the 2.5-hr sequence. [From S. J. Ostro, J. F. Chandler, A. A. Hine, I. I. Shapiro, K. D. Rosema, and D. K. Yeomans (1990). *Science* **248**, 1523–1528. Copyright 1990 AAAS.] (b) Three-dimensional computer model of Castalia, from inversion of the images in (a). The reconstruction uses 167 shape parameters and has a resolution of about 100 m. This contact-binary asteroid is about 1.8 km long. [From R. S. Hudson and S. J. Ostro (1994). *Science* **263**, 940–943. Copyright 1994 AAAS.]

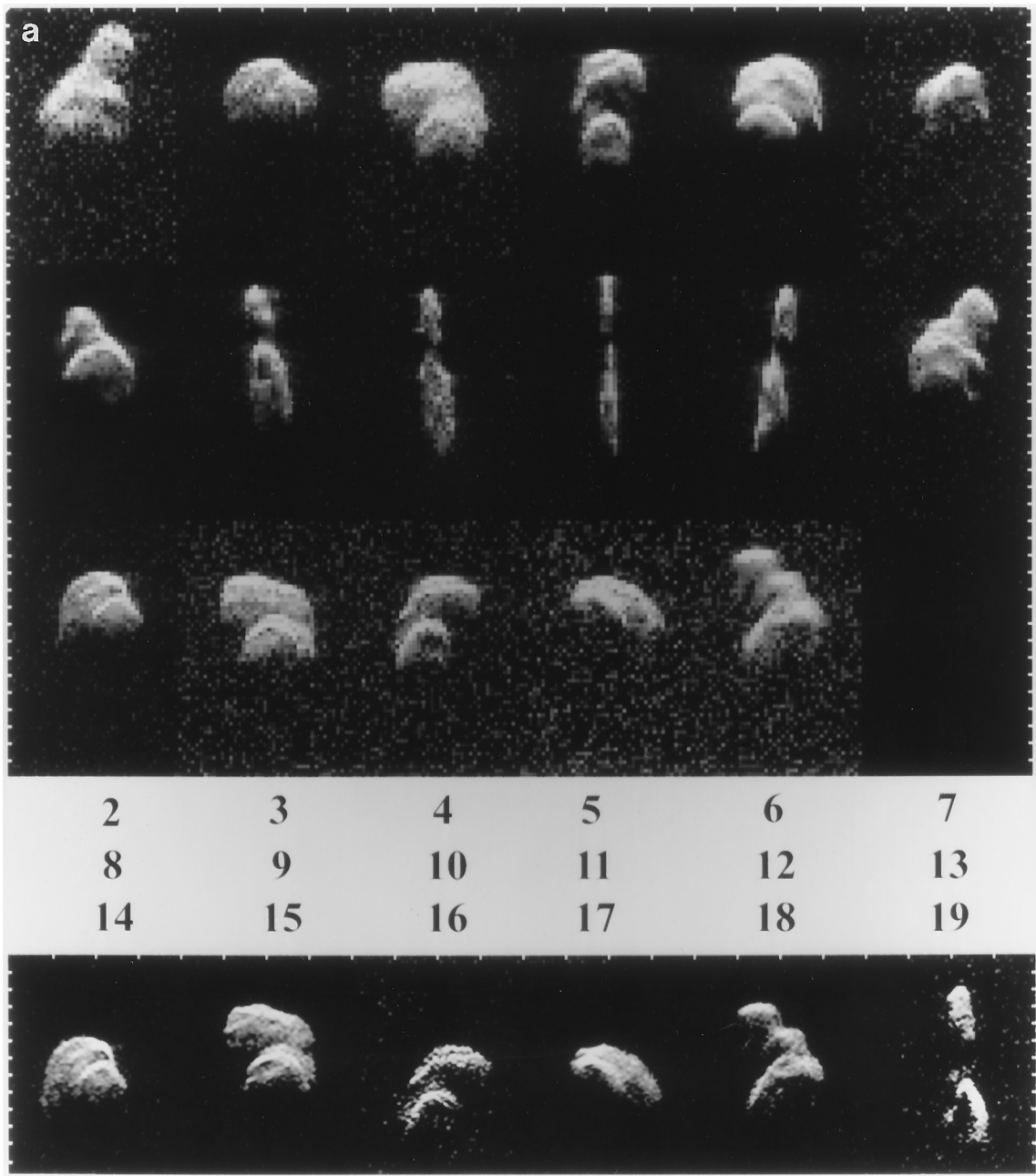


FIGURE 22 Radar images of near-Earth asteroid 4179 Toutatis. (a) Goldstone low-resolution images (top three rows) and Arecibo images (bottom row) obtained on the indicated dates in December 1992, plotted with time delay increasing toward the bottom and Doppler frequency increasing toward the left. On the vertical sides, ticks are $2\ \mu\text{sec}$ (300 m) apart. Two horizontal sides have ticks separated by 1 Hz for Goldstone and 0.28 Hz for Arecibo; those intervals correspond to a radial velocity difference of $18\ \text{mm sec}^{-1}$. (b) A high-resolution ($125\ \text{nsec} \times 33\ \text{mHz}$) Goldstone image obtained with Toutatis 3.6 million km (10 lunar distances) from Earth. The spatial resolution is $19 \times 46\ \text{m}$. [From S. J. Ostro *et al.* (1995). *Science* **270**, 80–83. Copyright 1995 AAAS.]

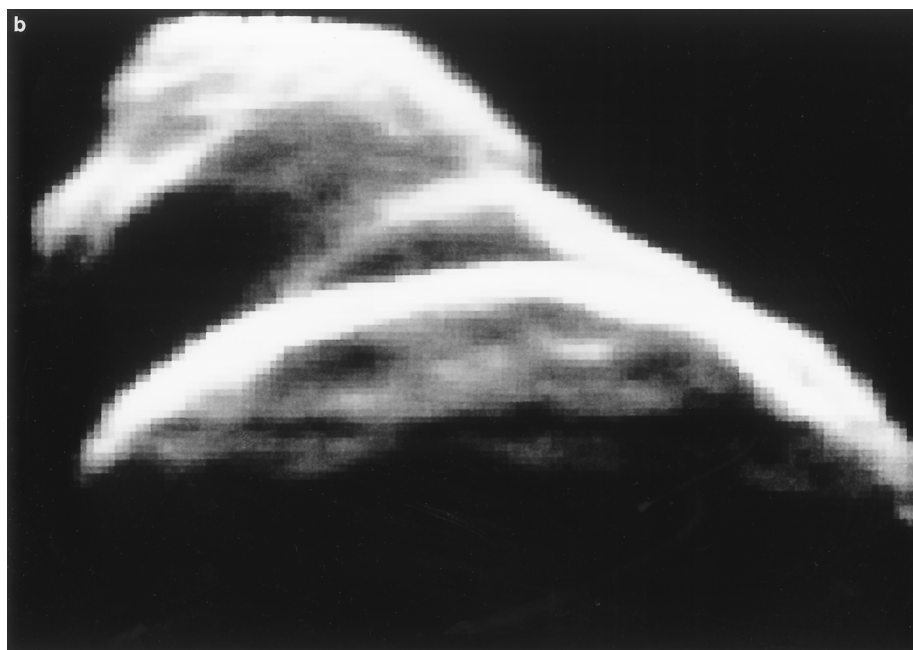


FIGURE 22 (continued)

nal structure. Simulations of impacts into Castalia using smooth-particle hydrodynamics code have begun to suggest how surface and interior damage depends on impact energy, impact location, and the equation of state of the asteroidal material. These computer investigations have clear ramifications for our understanding of asteroid collisional history, for exploitation of asteroid resources, and eventually for deflection/destruction of objects found to be on a collision course with Earth.

K. JUPITER'S ICY GALILEAN SATELLITES

Among all the radar-detected planetary bodies in the solar system, Europa, Ganymede, and Callisto have the most bizarre radar properties. Their reflectivities are enormous compared with those of the Moon and inner planets (see Table II). Europa is the extreme example (Fig. 24), with an OC radar albedo (1.0) as high as that of a metal sphere. Since the radar and optical albedos and estimates of fractional water frost coverage increase by satellite in the order Callisto–Ganymede–Europa, the presence of water ice has long been suspected of playing a critical role in determining the unusually high reflectivities even though ice is less radar-reflective than silicates. In spite of the satellites' smooth appearances at the several-kilometer scales of Voyager high-resolution images, a diffuse scattering

process and hence a high degree of near-surface structure at centimeter to meter scales is indicated by broad spectral shapes and large linear polarization ratios ($\mu_L \sim 0.5$).

The most peculiar aspect of the satellites' echoes is their circular polarization ratios, which exceed unity. That is, in contrast to the situation with other planetary targets, the scattering largely preserves the handedness, or helicity, of the transmission. Mean values of μ_C for Europa, Ganymede, and Callisto are about 1.5, 1.4, and 1.2, respectively. Wavelength dependence is negligible from 3.5 to 13 cm, but dramatic from 13 to 70 cm (Fig. 25). Significant polarization and/or albedo features are present in the echo spectra and in a few cases correspond to geologic features in Voyager images.

The icy satellites' echoes are due not to external surface reflections but to subsurface "volume" scattering. The high radar transparency of ice compared with that of silicates permits deeper radar sounding, longer photon path lengths, and higher-order scattering from regolith heterogeneities—radar is seeing Europa, Ganymede, and Callisto in a manner that the Moon has never been seen. The satellites' radar behavior apparently involves the coherent backscatter effect, which accompanies any multiple-scattering process; occurs for particles of any size, shape, and refractive index; and was first discovered in laboratory studies of the scattering of electrons and of light. Coherent

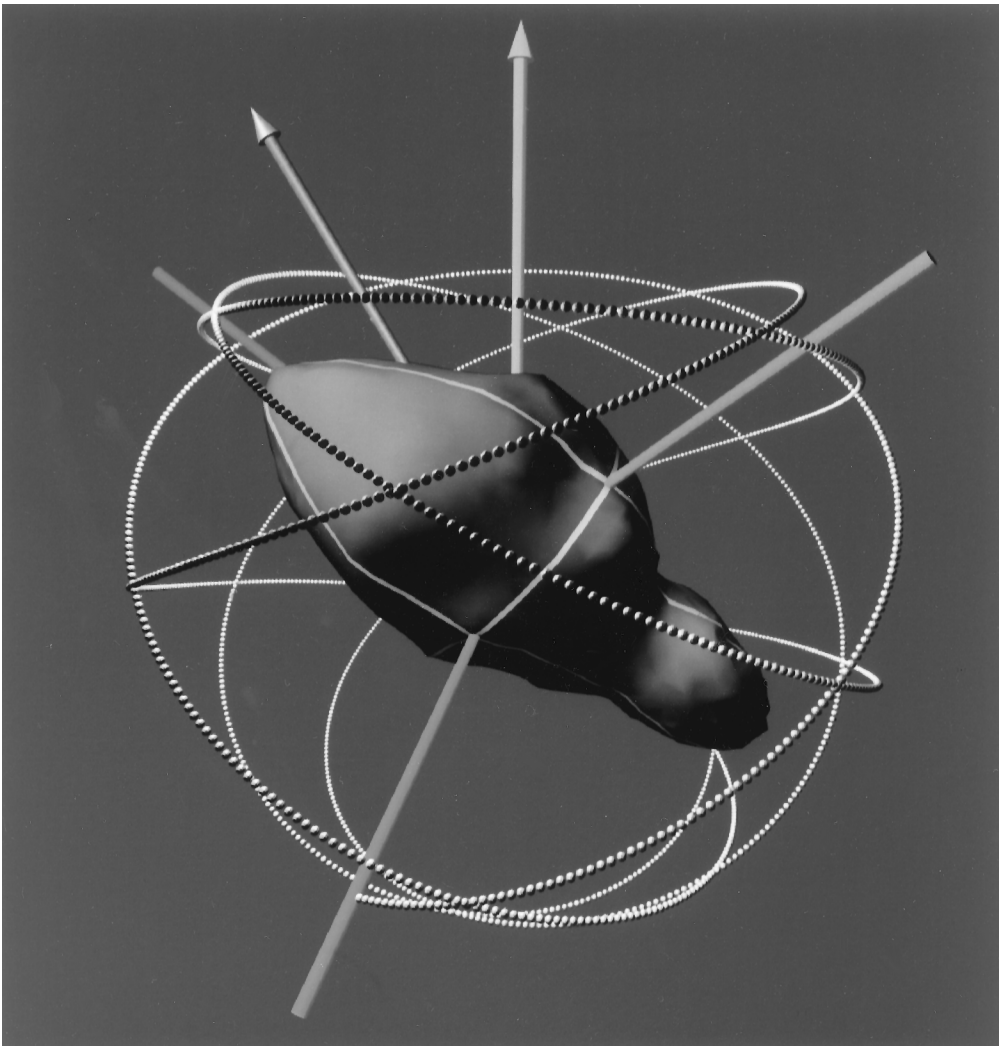


FIGURE 23 Toutatis’s shape and non-principal-axis spin state from inversion of the images in Fig. 21a. The axes with no arrow tips are the asteroid’s principal axes of inertia and the vertical arrow is its angular momentum vector; the direction of the spin vector (the arrow pointing toward eleven o’clock) relative to the principal axes is a (5.41-day) periodic function. A flashlamp attached to the short axis of inertia and flashed every 15 minutes for 20 days would trace out the intricate path indicated by the small spheres stacked end-to-end; the path never repeats. Toutatis’s spin state differs radically from those of the vast majority of solar system bodies that have been studied, which are in principal-axis spin states. For those objects, the spin vector and angular momentum vector point in the same direction and the flashlamp’s path would be a circle.

backscatter yields strong echoes and $\mu_C > 1$ because the incident, circularly polarized wave’s direction is randomized before its helicity is randomized and also before its power is absorbed. The vector-wave theory of coherent backscatter accounts for the unusual radar signatures in terms of high-order, multiple anisotropic scattering from within the upper few decameters of the regoliths, which the radar sees as an extremely low-loss, disordered random medium. Inter- and intrasatellite albedo variations show much more dynamic range than μ_C variations, and probably are due to variations in ice purity.

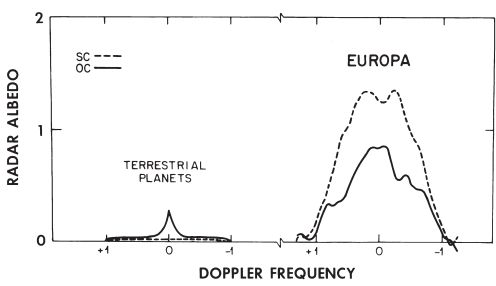


FIGURE 24 Typical 13-cm echo spectra for the terrestrial planets are compared to echo spectra for Jupiter’s icy moon Europa. The abscissa has units of half the echo bandwidth.

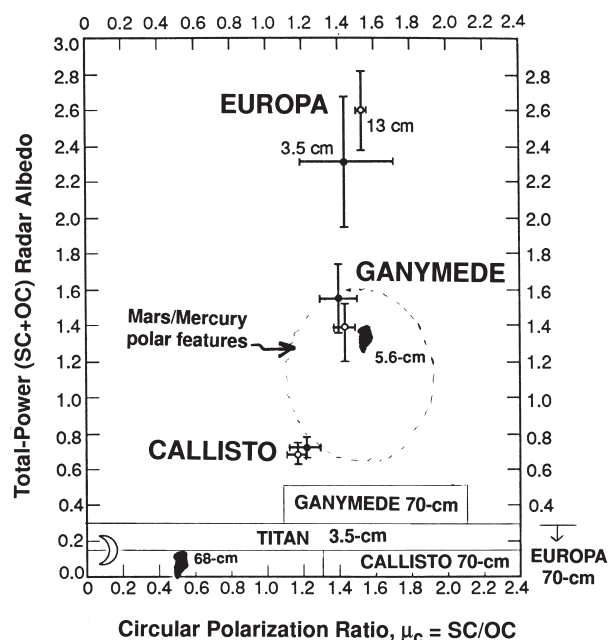


FIGURE 25 Radar properties of Europa, Ganymede, and Callisto compared to those of some other targets. The icy Galilean satellites' total-power radar albedos do not depend on wavelength between 3.5 and 13 cm, but plummet at 70 cm. There are large uncertainties in those objects' μ_C at 70 cm and in Titan's μ_C at 3.5 cm (the only wavelength at which it has been detected by radar). Solid symbols shaped like Greenland indicate properties of that island's percolation zone at 5.6 and 68 cm. The domain of most of the bright polar features on Mars and Mercury is sketched.

As sketched in Fig. 25, there are similarities between the icy Galilean satellites' radar properties and those of the radar-bright polar caps on Mars, features inside perpetually shadowed craters at the poles of Mercury (see Fig. 15), and the percolation zone in the Greenland ice sheet. However, the subsurface configuration in the Greenland zone, where the scattering heterogeneities are "ice pipes" produced by seasonal melting and refreezing, are unlikely to resemble those on the satellites. Therefore, unique models of subsurface structure cannot be deduced from the radar signatures of any of these terrains.

L. COMETS

Since a cometary coma is nearly transparent at radio wavelengths, radar is much more capable of unambiguous detection of a cometary nucleus than are optical and infrared methods, and radar observations of several comets (see Table I) have provided useful constraints on nuclear dimensions. The radar signature of one

particular comet (IRAS-Araki-Alcock, which came within 0.03 AU of Earth in May 1983) revolutionized our concepts of the physical nature of these intriguing objects. Echoes obtained at both Arecibo (Fig. 26) and Goldstone have a narrowband component from the nucleus as well as a much weaker broadband component from large particles ejected mostly from the sunlit side of the nucleus. Models of the echoes suggest that the nucleus is very rough on scales larger than a meter, that its maximum overall dimension is within a factor of two of 10 km, and that its spin period is 2–3 days. The particles are probably several centimeters in size and account for a significant fraction of the particulate mass loss from the nucleus. Most of them appear to be distributed within ~ 1000 km of the nucleus, that is, in the volume filled by particles ejected at several meters per second over a few days. The typical particle lifetime may have been this short, or the particle ejection rate may have been highly variable.

In late 1985, radar observations of comet Halley, which was much more active than IRAS-Araki-Alcock, yielded echoes with a substantial broadband component presumed to be from a large-particle swarm, but no narrowband component, a negative result consistent with the hypothesis that the surface of the nucleus has an extremely low bulk density. In 1996, Goldstone obtained 3.5-cm echoes from the nucleus and coma of comet Hyakutake (C/1996 B2). The coma-to-nucleus ratio of radar cross section is about 12 for Hyakutake versus about 0.3 for IAA. The radar signatures of these three comets strengthen impressions about the diversity, and unpredictability, of comet physical properties

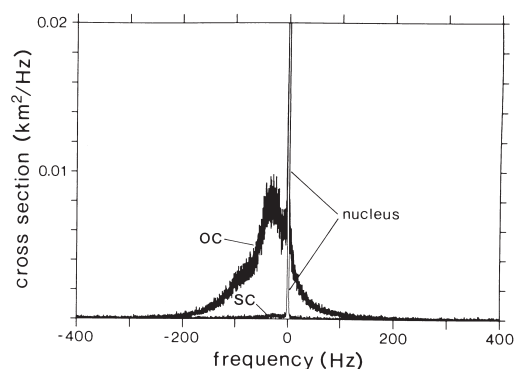


FIGURE 26 OC and SC echo spectra obtained at 13 cm for comet IRAS-Araki-Alcock, truncated at 2% of the maximum OC amplitude. The narrowband echo from the nucleus is flanked by a broadband echo from large (1-cm) particles in a 1000-km-radius cloud surrounding the nucleus. [From J. K. Harmon, D. B. Campbell, A. A. Hine, I. I. Shapiro, and B. G. Marsden (1989). *Astrophys. J.* **338**, 1071–1093.]

and have obvious implications for spacecraft operations close to comets.

M. SATURN'S RINGS AND TITAN

The only radar-detected ring system is quite unlike other planetary targets in terms of both the experimental techniques employed and the physical considerations involved. For example, the relation between ring-plane location and delay-Doppler coordinates for a system of particles traveling in Keplerian orbits is different from the geometry portrayed in Fig. 5. The rings are grossly overspread (see Table II), requiring the use of frequency-stepped waveforms in delay-Doppler mapping experiments.

Radar determinations of the rings' backscattering properties complement results of the Voyager spacecraft radio occultation experiment (which measured the rings' forward scattering efficiency at identical wavelengths) in constraining the size and spatial distributions of ring particles. The rings' circular polarization ratio is ~ 1.0 at 3.5 cm and ~ 0.5 at 13 cm, more or less independent of the inclination angle δ between the ring plane and the line of sight. Whereas multiple scattering between particles might cause some of the depolarization, the lack of strong dependence of μ_C on δ suggests that the particles are intrinsically rougher at the scale of the smaller wavelength. The rings' total-power radar albedo shows only modest dependence on δ , a result that seems to favor many-particle-thick models of the rings over monolayer models. Delay-Doppler resolution of ring echoes indicates that the portions of the ring system that are brightest optically (the A and B rings) also return most of the radar echoes. The C ring has a very low radar reflectivity, presumably because of either a low particle density in that region or compositions or particle sizes that lead to inefficient scattering.

Apart from landing a spacecraft on Titan, radar provides the most direct means to study the cloud-covered surface of Saturn's largest moon. Voyager and ground-based data indicate a surface temperature and pressure of 94 K and 1.5 bar, and show that the atmosphere is mostly N₂ with traces of hydrocarbons and nitriles. Thermodynamic considerations imply a near-surface reservoir of liquid hydrocarbons, possibly consisting of a kilometer-deep global ocean. However, that configuration, which would give a radar albedo of only several percent, has been ruled out by Goldstone-VLA detections that yield OC albedo estimates that

average about 0.13. More work is needed to elucidate Titan's radar properties.

IV. PROSPECTS FOR PLANETARY RADAR
.....

The 1993–1997 upgrading of the Arecibo telescope has increased the instrument's average radar sensitivity by a factor of 20, more than doubling its range and reducing by nearly an order of magnitude the diameter of the smallest object detectable at any given distance. The impact of the Arecibo upgrade on planetary science is expected to be fundamental and far-reaching, especially for studies of small bodies and planetary satellites. The quality, in terms of signal-to-noise ratio and spatial resolution, of radar measurements will jump by more than an order of magnitude. Several short-period comets will become easy targets. The pre-upgrade Arecibo could barely skim the inner edge of the main asteroid belt, but the upgraded telescope will have access to asteroids throughout the belt. The instrument is expected to provide high-resolution images of dozens of asteroids per year.

Efforts are under way to increase the near-Earth asteroid discovery rate by one to two orders of magnitude. Most of the optically discoverable NEAs traverse the detectability windows of the upgraded Arecibo and/or Goldstone telescopes at least once during any given several-decade interval. In view of the utility of radar observations for orbit refinement and physical characterization, there is considerable motivation to do radar observations of newly discovered NEAs whenever possible. The initial radar reconnaissance of a new NEA might eventually become an almost daily opportunity.

Radar investigations of natural satellites will reap enormous benefits from ground-based and spaceborne radar reconnaissance. The near-surface physical properties of Deimos, Io, and Titan will be readily discernible with Arecibo. Doppler images of Titan may furnish a coarse-resolution, nearly global albedo map, while the *Cassini* spacecraft, with its high-resolution, 13.8-GHz (2.2-cm) radar instrument, is journeying toward its arrival at Saturn in 2004. That instrument, which will function as a synthetic-aperture radar imager, an altimeter, and a passive radiometer, is designed to determine whether oceans exist on Titan, and, if so, to determine their distribution. There is growing interest in the possibility of a subsurface ocean on Europa, and in the feasibility of using an orbiting, long-wavelength (~ 6 -m) radar sounder to probe many

kilometers below that object’s fractured crust, perhaps within a decade. In summary, planetary radar astronomy appears to be on the verge of producing an enormously valuable body of new information about asteroids, comets, and the satellites of Mars, Jupiter, and Saturn.

BIBLIOGRAPHY

Butrica, A. J. (1996). “To See the Unseen: A History of Planetary Radar Astronomy,” NASA History Series No. SP-4218. NASA, Houston.

Harmon, J. K., Slade, M. A., Velez, R. A., Crespo, A., Dryer, M. J., and Johnson, J. M. (1994). Radar mapping of Mercury’s polar anomalies. *Nature* **369**, 213–215.

Hudson, R. S., and Ostro, S. J. (1995). Shape and non-principal axis spin state of asteroid 4179 Toutatis. *Science* **270**, 84–86.

Mitchell, D. L., Ostro, S. J., Hudson, R. S., Rosema, K. D., Campbell, D. B., Velez, R., Chandler, J. F., Shapiro, I. I., Giorgini, J. D., and Yeomans, D. K. (1996). Radar observations of asteroids 1 Ceres, 2 Pallas, and 4 Vesta. *Icarus* **124**, 113–133.

Muhleman, D. O., Grossman, A. W., and Butler, B. J. (1995). Radar

investigation of Mars, Mercury, and Titan. *Annu. Rev. Earth Planet Sci.* **23**, 337–374.

Ostro, S. J. (1993). Planetary radar astronomy. *Rev. Modern Physics* **65**, 1235–1279.

Pettengill, G. H., Ford, P. G., Johnson, W. T. K., Raney, R. K., and Soderblom, L. A. (1991). Magellan: Radar performance and data products. *Science* **252**, 260–265.

Shapiro, I. I., Chandler, J. F., Campbell, D. B., Hine, A. A., and Stacy, N. J. S. (1990). The spin vector of Venus. *Astron. J.* **100**, 1363–1368.

Simpson, R. A., Harmon, J. K., Zisk, S. H., Thompson, T. W., and Muhleman, D. O. (1992). Radar determination of Mars radar properties. *In* “Mars” (H. Kieffer, B. Jakosky, C. Snyder, and M. Matthews, eds.), pp. 652–685. Univ. Arizona Press, Tucson.

Slade, M. A., Butler, B. J., and Muhleman, D. O. (1992). Mercury radar imaging: Evidence for polar ice. *Science* **258**, 635–640.

Stacy, N. J. S., Campbell, D. B., and Ford, P. G. (1997). Arecibo radar mapping of the lunar poles: A search for ice deposits. *Science* **276**, 1527–1530.

Tyler, G. L., Ford, P. G., Campbell, D. B., Elachi, C., Pettengill, G. H., and Simpson, R. A. (1991). Magellan: Electrical and physical properties of Venus’ surface. *Science* **252**, 265–270.

Yeomans, D. K., Chodas, P. W., Keesey, M. S., Ostro, S. J., Chandler, J. F., and Shapiro, I. I. (1992). Asteroid and comet orbits using radar data. *Astron. J.* **103**, 303–317.